Supporting Information

accompanying the manuscript

Fundamental Structure and Modulation of Neuronal Excitability: Synaptic Control of Coding, Resonance, and Network Synchronization

Christoph Kirst[1,2], *Julian Ammer*[1,3], *Felix Felmy*[1,4], *Andreas Herz*[1,3,5], *Martin Stemmler*[1,5]

[1]Ludwig-Maximilians-University Munich, Dept. Biology II, Germany

[2]The Rockefeller University, Center for Physics and Biology, New York, USA

[3]Graduate School for Systemic Neurosciences, LMU Munich, Germany

[4]Ludwig-Maximilians-University Munich, Dept. Biology I, BioImaging Zentrum, Germany

[5]Bernstein Center for Computational Neuroscience Munich, Germany

1 Supplementary Figures

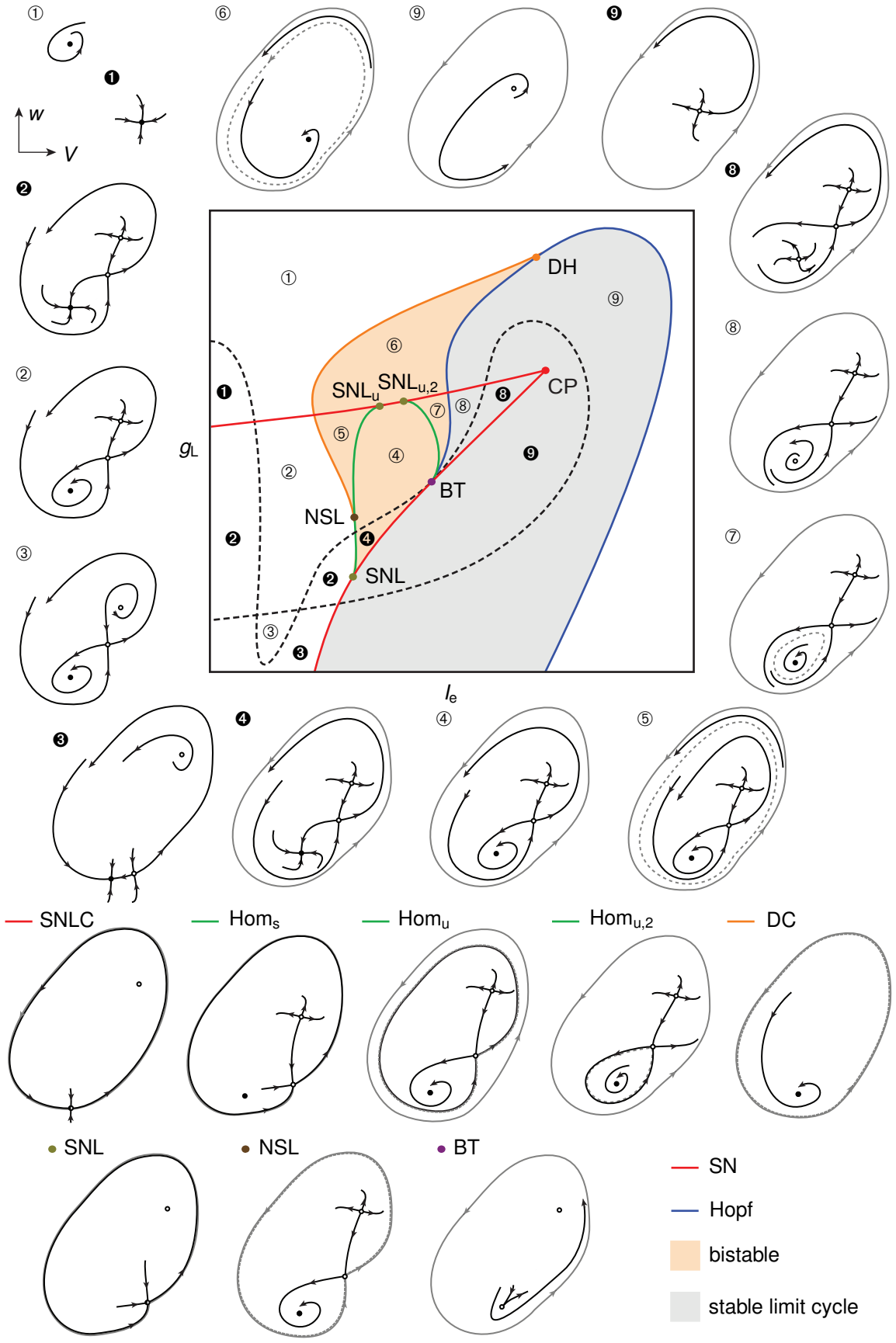

Supplementary Figure S1: *Organization of leak-induced neuronal excitability transitions by a Bogdanov-Takens-Cusp bifurcation.*

Supplementary Figure S1 (caption continued):
Schematic two-dimensional section through the 3-parameter unfolding of a Bogdanov-Takens-cusp bifurcation of focus type (cf. Fig. 2 and [1]) with sketches of the corresponding phase plane dynamics. The horizontal axis represents the input current I_e, the vertical axis the leak conductance g_L. The different phase plane dynamics are sketched in the two-dimensional center manifold with the membrane-potential V and an effective delayed rectifier variable w as coordinates. In the bifurcation diagram, solid lines represent co-dimension 1 and points co-dimension 2 bifurcations. Within the unshaded region, no spikes occur; the gray area( ) corresponds to stable periodic spiking; while orange shading ( ) denotes bi-stability between resting and stable periodic spiking; The dashed line (--) represents a node-to-focus transition where the linearized dynamics around the fixed points become oscillatory, as the eigenvalues change from being purely real (node) to becoming complex (focus). In the sketches, stable (unstable) fixed points are indicated by filled (open) dots and stable (unstable) limit cycles by solid (dashed) gray lines. Lines with arrows represent parts of (un)stable manifolds of the fixed points.
Various co-dimension 2 bifurcations organize the individual transitions steps in the bifurcation diagram: The saddle node loop bifurcation (SNL, •) organizes a switch from a saddle node on limit cycle (SNLC, –, below •) to a homoclinic ($\mathrm{Hom_s}$, –) and a saddle-node (SN, –, above •) bifurcation. The neutral saddle loop bifurcation (NSL, •) splits the homoclinic that yields a stable limit cycle ($\mathrm{Hom_s}$, –) into a double limit cycle (DC, –) and a homoclinic bifurcation involving an unstable cycle ($\mathrm{Hom_u}$, –). Finally the DC bifurcation changes via a degenerate Hopf (DH, •) to an ordinary Hopf bifurcation (–). The Bogdanov-Takens bifurcation (BT, •) organizes a change from saddle node (SN,–) to Hopf (–) and homoclinic ($\mathrm{Hom_{u,2}}$, –) bifurcations. The node-to-focus transition (--), which is related to the change in membrane resonance, passes through the BT point tangentially to the other bifurcation lines.
The numerically calculated global bifurcation diagrams for the unfolding of an elliptic Bogdanov-Takens-cusp point have the same topology as the focus type shown here; in the elliptic sub-type example shown in Fig. S3G-I, region ⑤ almost vanishes.

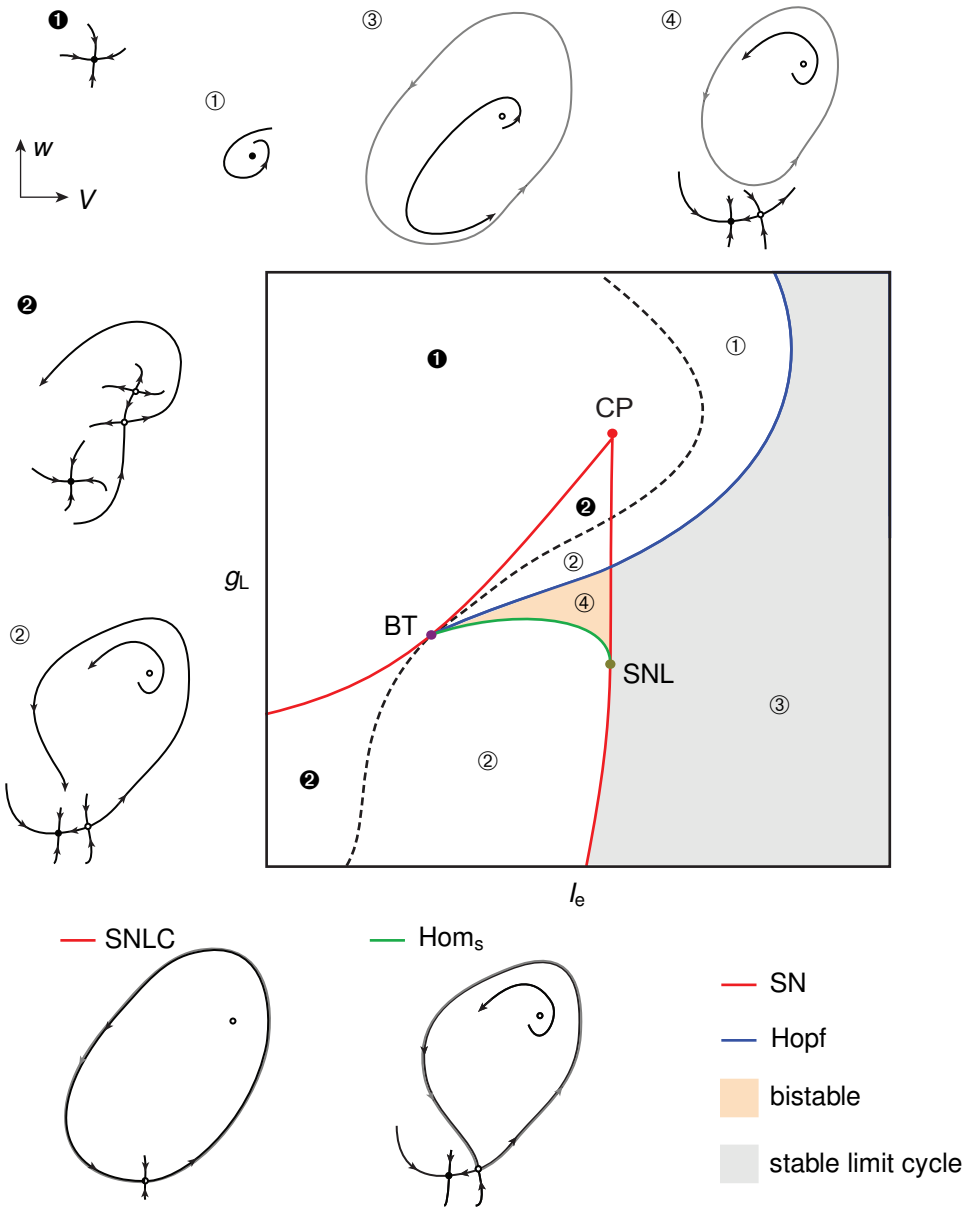

Supplementary Figure S2:
Organization of leak-induced neuronal excitability transitions by a Bogdanov-Takens-Cusp Bifurcation for High capacitances.
Increasing the capacitance past the BTC point (cf. Fig. 2C) changes the two- dimensional section through the 3-parameter unfolding of the Bogdanov-Takens-cusp (BTC) bifurcation of focus type. In contrast to Fig. S1, the Bogdanov-Takens bifurcation (BT, •) has moved to the branch of the saddle-node bifurcations (SN, –) that is to the left of the cusp (CP, •). The homoclinic (Hom_s, –) bifurcation generates a stable limit cycle that only encircles the upper focus but not the other fixed points. Colors as in Fig. S1.

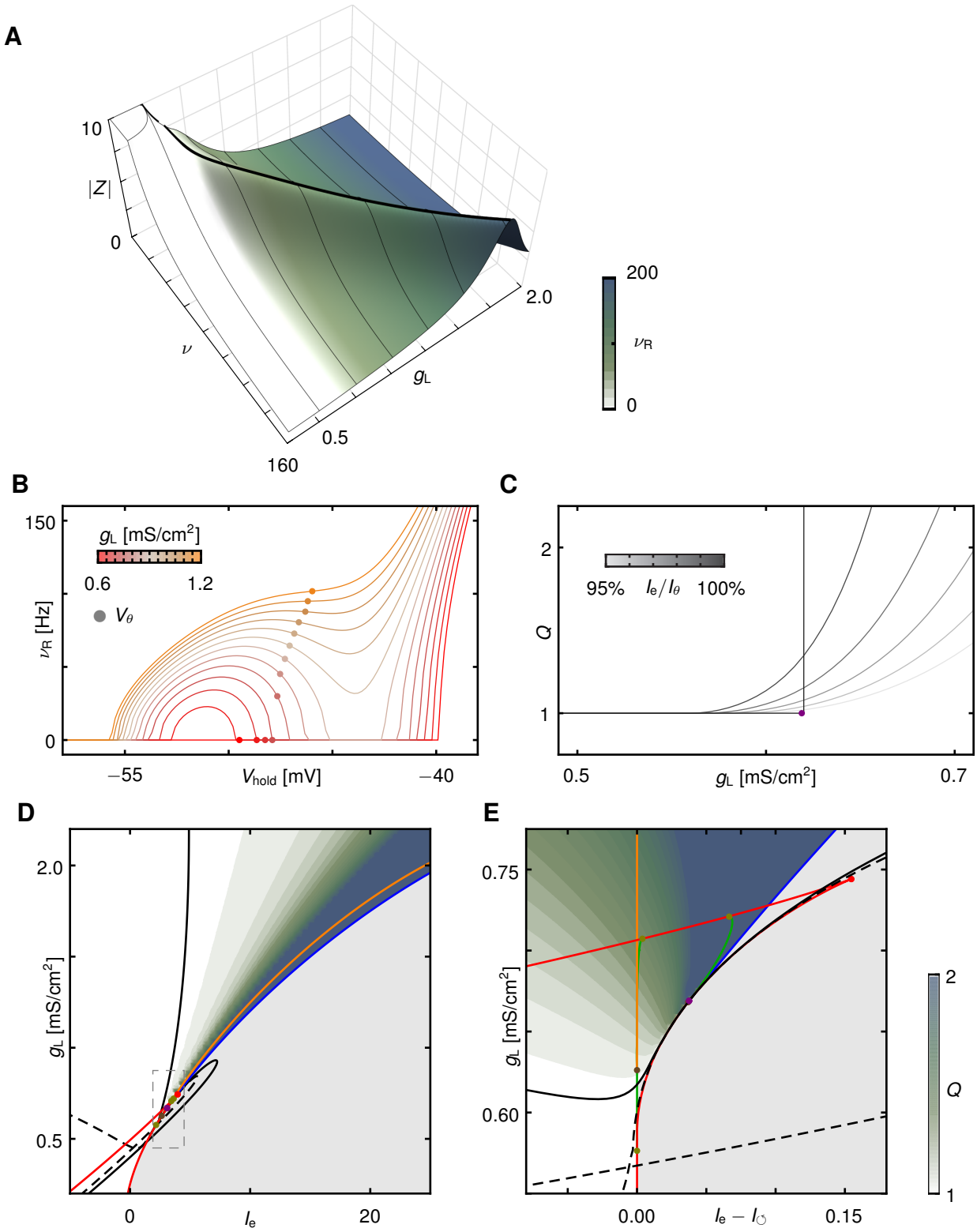

Supplementary Figure S3:
Leak-induced transition to membrane-potential resonance in model neurons.
As the leak conductance g_L in the Wang-Buzsaki model [2] increases resonance properties emerge in addition to the changes in neuronal excitability (cf. also Figs. 1-3 in the main manuscript).

Supplementary Figure S3 (caption continued):
(A) Linear response $|Z|$ at 95% of the AP onset current. The curves change from monotonically decaying to uni-modal with resonance frequency at the maximum (black line). Resonance frequency ν_{R} color-coded as in Fig. 2D.
(B) Resonance frequency ν_{R} as a function of the holding membrane potential V_{hold} for leak conductances ranging from 0.6 to 1.2 $\mathrm{mS/cm^2}$ in steps of 0.05 $\mathrm{mS/cm^2}$. Filled dots on the curves indicate the membrane threshold V_θ at which the neuron starts spiking due to destabilization of the fixed point. The dependence of ν_{R} on V_{hold} is non-monotonic for leak values below and close to the BT point (cf. Fig. 2, S4, and S6). In this region, the saddle-node bifurcation marks the onset of AP generation and the initial rise in ν_{R} must be followed by a decay to zero as the AP threshold is approached, because at the saddle-node the eigenvalues of the linearized system are real and not complex. In view of the (I_{e},g_{L})-parameter space (cf. Fig. 2 and S1) the initial rise ν_{R} originates from the transition to resonance curve (dashed line, --) becoming tangential to the saddle-node line at the BT point giving rise to a region of resonance even below the BT point. The graph highlights two effects by which the addition of a leak conductance changes the resonance frequency: First, for fixed V_{hold}, increasingg_{L}, hastens the speed with which the membrane voltage recovers from deflections and thereby increases ν_{R}. Second, increasing g_{L} moves the potential threshold V_θ upwards and thereby exerts an indirect effect on the measured resonance frequency at threshold $\nu_{\mathrm{R},0}$.
(C) Q-factor $Q = |Z(\nu_{\mathrm{R}})/Z(0)|$ as a function of the leak conductance g_{L}. The Q-factor measures the amplitude of the response Z at the resonance frequency ν_{R} relative to the steady-state amplitude $|Z(0)|$. Q is shown for different currents I_{e} that are fixed fractions of the threshold current I_θ for AP generation, ranging from 95% (light gray) to 100% (black). At 100% of the threshold current the Bodgdanov-Takens bifurcation point (BT, •) marks the onset of resonance at zero frequency; however, the linearized dynamics are no longer bounded and thus linear response theory predicts a diverging Q-Factor. The dynamics of the full nonlinear model will, of course, remain bounded.
(D,E) The Q-factor $Q = |Z(\nu_{\mathrm{R}})/Z(0)|$ as a function of the input current I_{e} and g_{L}. Bifurcations lines are as in Fig. 2B. Q-factors are shown with an upper cut off at 2. The linear response and Q diverge at spike onset (see black line in B).

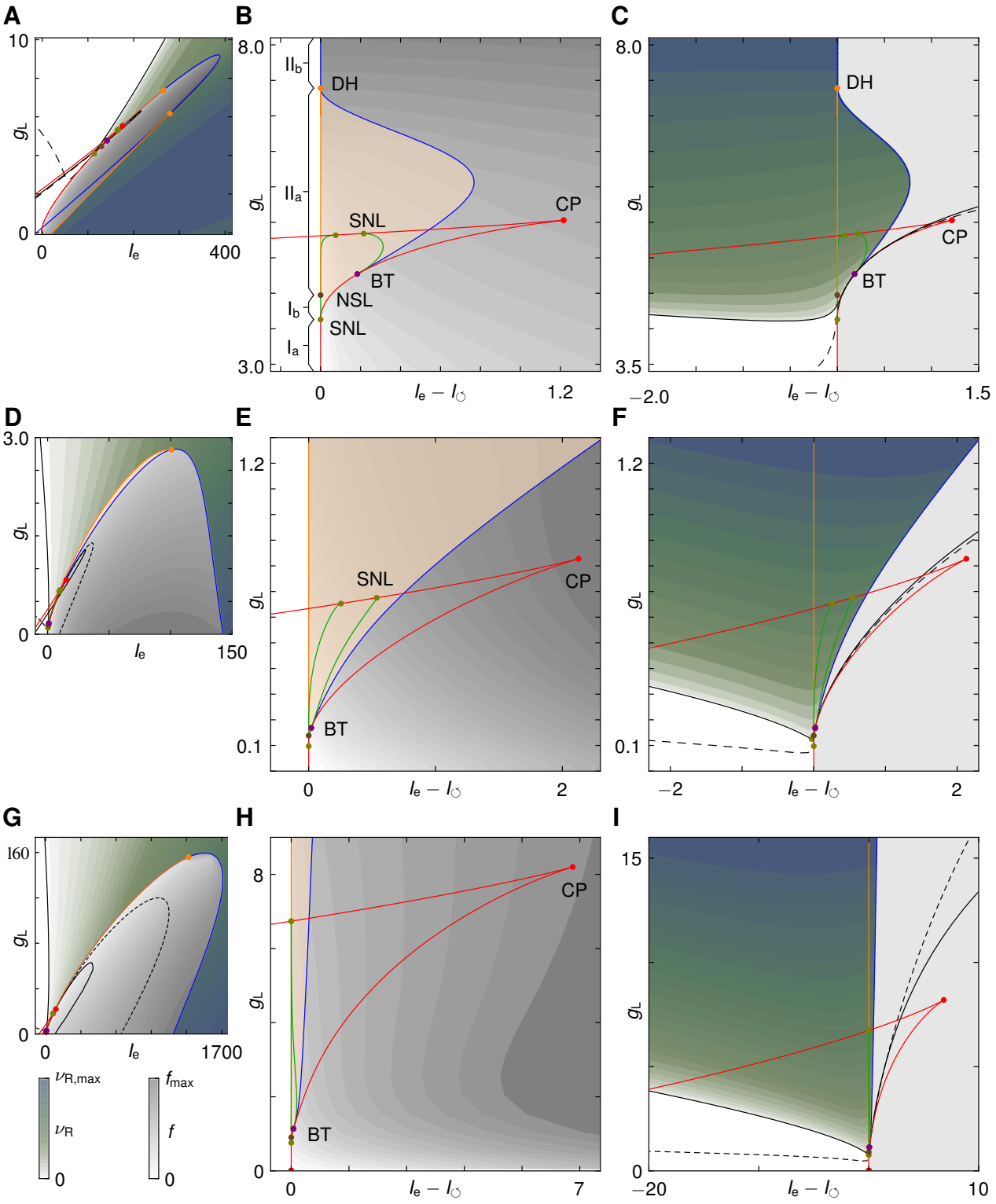

Supplementary Figure S4:
Prevalence and generality of leak-induced neuronal excitability and resonance transitions in neuron models.

Supplementary Figure S4 (caption continued):
Shown are the bifurcation diagrams together with spike and resonance frequencies in the I_e-g_L-parameter plane for three different neuron models. All exhibit the same pattern of leak-induced transitions as observed for the Wang-Buzsaki neuron model shown in Fig. 2 and S1. I_e is measured in $\mu A/cm^2$ and g_L in mS/cm^2.
(A-C) Leak-induced transitions in the Morris-Lecar neuron model [3]. (A) bifurcation diagram for the the entire region of spiking dynamics. The spiking frequency f is indicated by gray shading (maximal spiking frequency $f_{max} = 33.9\,Hz$). For stable fixed points the resonance frequency ν_R, as determined by linear response theory, is shown in alpine colors (maximal resonance frequency is $\nu_{R,max} = 47.8\,Hz$). Colored lines indicate the co-dimension 1 bifurcations: saddle node or saddle node on invariant cycle (–), homoclinic (–), Hopf (–) and double limit cycle (–). Points are the co-dimension 2 bifurcations: cusp (CP, •) Bogdanov-Takens, (BT, •), neutral saddle loop (NSL, •), saddle node loop (SNL, •) and degenerate Hopf (DH, •) (cf. Suppl. Fig. S1). Black dashed line (--) demarcates the transition in which two eigenvalues of the linearized dynamics become a complex conjugate pair, indicative of oscillatory ringing in the membane potential. Black solid line (—) shows the transitions from monotonically decaying to non-monotonic peaked amplitudes $|Z|$ of the transfer functions Z, as obtained by linear response theory. A peaked $|Z|$ indicates resonance. The diagram shows that increasing leak not only induces a switch in neuronal excitability, but also in resonance, which first appears entirely within the sub-threshold regime. (B) close-up of the transition area ($f_{max} = 18.5\,Hz$). The current I_e is shifted by the current $I_{\circlearrowleft}$ at onset of periodic spiking. Orange shading (▭) indicates the region of bi-stability between stable spiking and resting. (C) close-up highlighting the region of sub-threshold resonance ($\nu_{R,max} = 17.1\,Hz$). The curve marking the transition to resonance (—) passes the BT point and runs parallel to the Hopf and saddle node lines. Near the BT point, this results in a non-monotonic dependence of the resonance frequency $\nu_0\,(I_e)$ on I_e for fixed g_L as it first rises then falls as I_e increases towards the spiking threshold (cf. also Fig. S3).
(D-F) as in (A-C) for a fast spiking inter-neuron model [4]. Maximal frequencies are (D) $f_{max} = 251.7\,Hz$ and $\nu_{R,max} = 263.7\,Hz$, (E) $f_{max} = 90.5\,Hz$, (F) $\nu_{R,max} = 46.0\,Hz$
(G-I) as in (A-C) for a reduced pyramidal neuron model [5, 6]. Maximal frequencies are (G) $f_{max} = 2315\,Hz$ and $\nu_{R,max} = 2110\,Hz$, (H) $f_{max} = 311.6\,Hz$, (I) $\nu_{R,max} = 377.0\,Hz$. High frequencies arise as APs change to very fast small-amplitude oscillations for very high leak conductances or high inputs currents near the conductance block.
All diagrams, including the Wang-Buzsáki neuron model in Fig. 2, share the same topology. In the supplementary text, we prove that leak-induced excitability and resonance transitions in class-I conductance-based neuron models possess a Bogdanov-Takens-cusp point of focus or elliptic type whose unfolded bifurcation diagrams have the topology observed here and in Fig. 2, S1, S5 and S6.

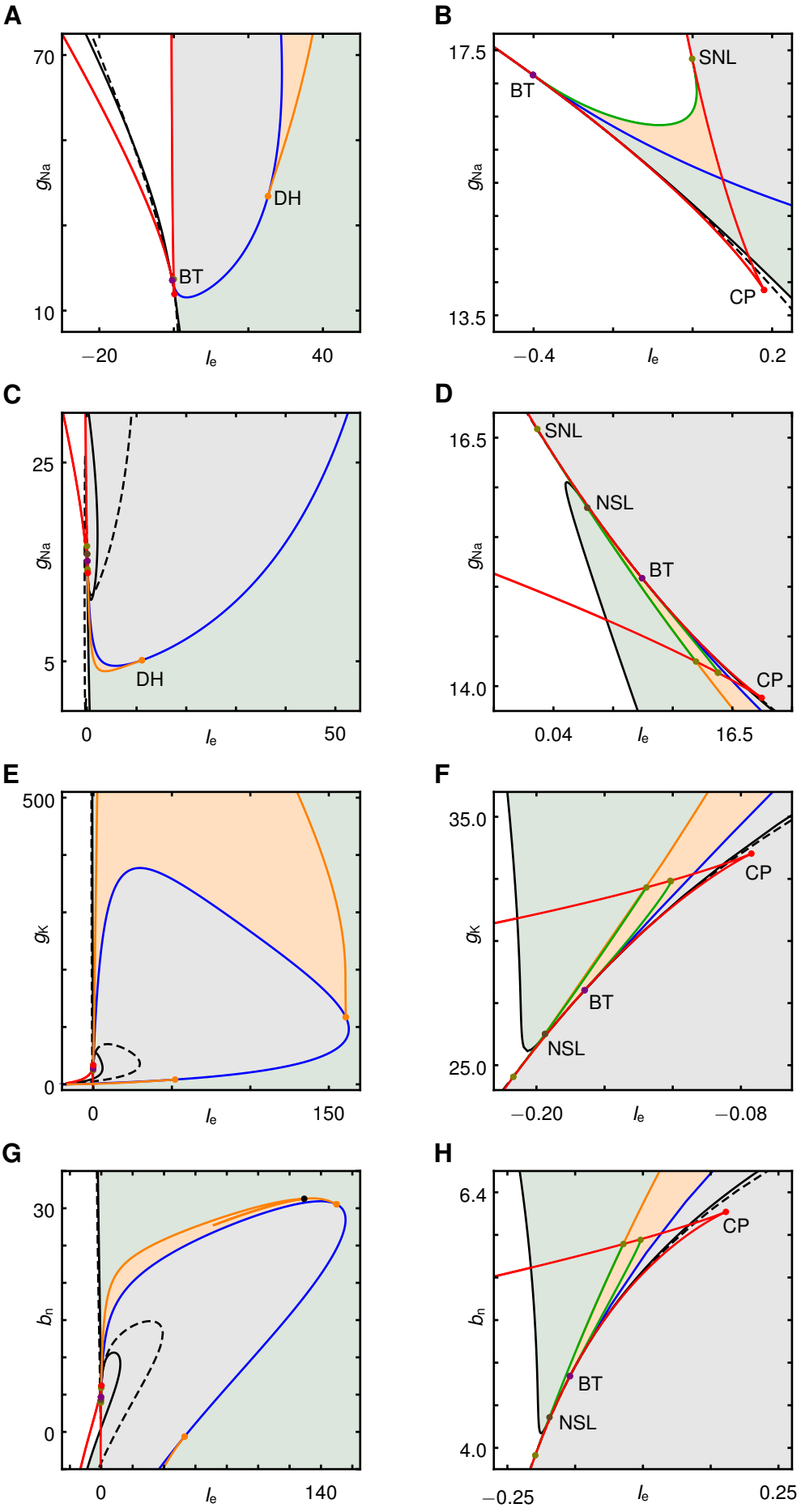

Supplementary Figure S5:
Neuronal excitability and resonance transitions induced by changes in ion-channel parameter.

Supplementary Figure S5 (caption continued):
The BTC point not only organizes leak-induced neuronal excitability transitions but more generally captures the transitions induced by arbitrary changes in the AP generating ion-channel parameters. Shown are bifurcation diagrams for different parameter planes in the Wang-Buzsaki model [2]. Bifurcation lines and labels as in Fig. S1, S3, S4. Green shading denotes the presence of resonance. I_e is measured in $\mu A/cm^2$, g_{Na} and g_K in mS/cm^2 and b_n in mV.
(A,B) Coarse and fine-scale bifurcation diagram in the input current I_e and maximal sodium conductance g_{Na} plane. The structure is equivalent to a section in the three dimensional (I_e, g_L, c_m)-bifurcation diagram (Fig. 2C) for constant c_m above the BTC point (cf. Fig. S2). The sodium current is directed inwards, in the opposite direction of the leak, which inverts the ordinate axis compared to Fig. 2 .
(C,D) as in (A,B) for smaller $c_m = 0.2\,\mu F/cm^2$. The diagram has exactly the transition structure as observed for the $I_e - g_L$-bifurcation diagrams (cf. Fig. 2 and S1) whit reversed ordinate axis.
(E,F) Bifurcation diagram in the input current I_e and maximal potassium conductance g_K for $c_m = 0.2\,\mu F/cm^2$. The delayed rectifier and leak currents are both outward; the bifurcation diagram hence has the same orientation as the $I_e - g_L$-bifurcation diagram.
(G,H) Bifurcation diagram in the input current I_e and half-activation voltage of the potassium conductance b_n for $c_m = 0.2\,\mu F/cm^2$. the transition structure of the $I_e - g_L$-bifurcation diagram below the BTC point (cf. Fig. 2 and S1).
For $c_m = 1.0\,\mu F/cm^2$, all diagrams have a transition structure as in (A,B) (not shown).

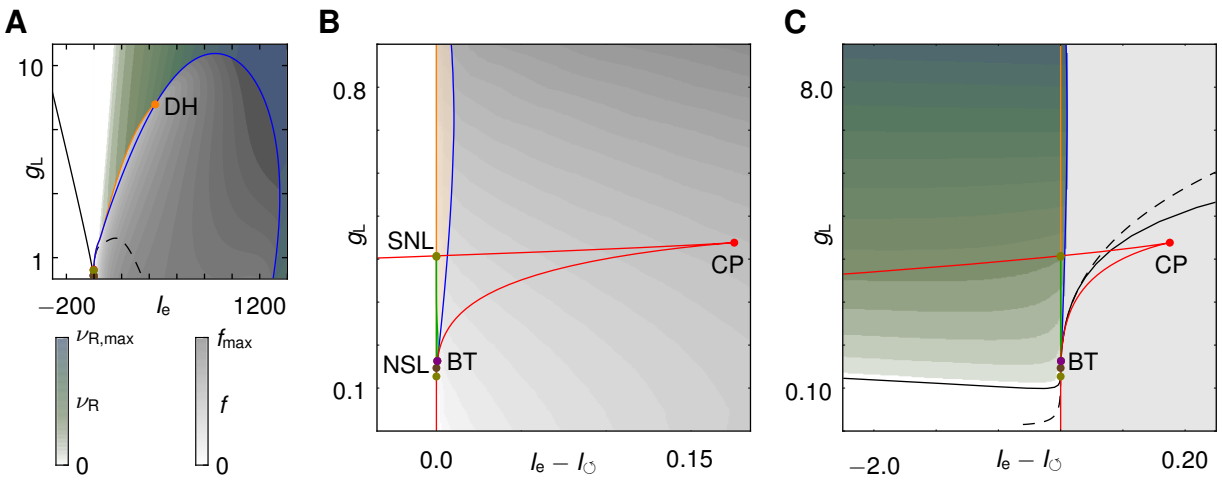

Supplementary Figure S6:
Leak-induced neuronal excitability transitions and adaptation
Bifurcation diagrams together with spike and resonance frequencies in the I_e-g_L-parameter plane for a Morris-Lecar neuron model with an additional adaptation current [7]. Adaptation causes the firing rate upon sustained current injection to slow down and is a characteristic feature of regularly spiking cells. The BTC structure persists, with one exception: for leak conductances above $g_L \approx 0.4$ mS/cm^2 and below the degenerate Hopf point (DH) the onset of spiking with a non-zero frequency interacts with the adaptation currents that act on a slower time scale. Thus, the transition to spiking no longer occurs through a single double limit cycle (DC) bifurcation but rather a sequence of complex transitions involving period-doublings. Large-scale voltage excursions mixed with sub-threshold oscillations appear in the vicinity of what used to be the DC line. The maximal and minimal spiking and resonance frequencies displayed within each diagram are (A) $f_{max} = 544$ Hz and $\nu_{R,max} = 536$ Hz, (B) $f_{max} = 6.1$ Hz, (C) $\nu_{R,max} = 8.6$ Hz. Eliminating the adaptation current changes the BT point from $g_L \approx 0.18$ to $g_L \approx 2.165$ mS/cm^3 but leaves the overall bifurcation structure unchanged (not shown).

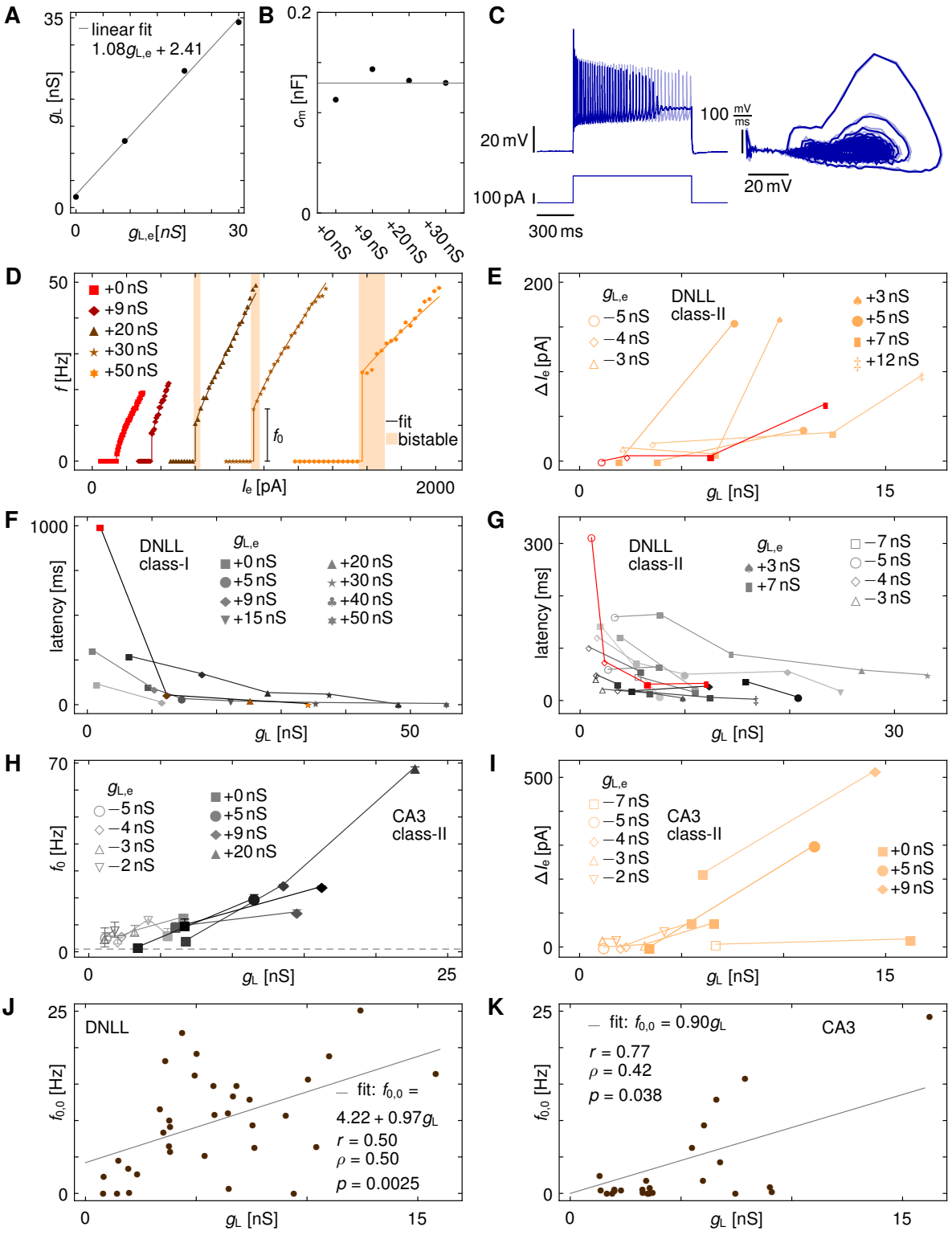

Supplementary Figure S7

Leak-induced neuronal excitability transition and bistability in DNLL and CA3 neurons.

Supplementary Figure S7 (caption continued):
(A) Measured leak g_{L} as a function of the externally applied leak $g_{\mathrm{L,e}}$ for the neuron shown in Fig. 4A. The external leak provided by dynamic clamp is additive, as evidenced by the graph's linear relationship with a slope close to unity. Across all cells studied, the fit was linear with slopes varying between 0.85 and 1.35.
(B) Measured capacitance c_{m} as a function of the externally applied leak $g_{\mathrm{L,e}}$ for the neuron shown in Fig. 4A. The capacitance stays nearly constant during the experiment. This behavior is observed for all cells, with variations that are within 30% of the control capacitance.
(C) Spiking dynamics of the neuron in Fig. 4A for $I_{\mathrm{e}} = 1220\,\mathrm{pA}$ (light blue) and $I_{\mathrm{e}} = 1240\,\mathrm{pA}$ (blue). The higher input current caused a conductance block and the neuron stopped firing periodic APs. The AP amplitudes for $I_{\mathrm{e}} = 1220\,\mathrm{pA}$ decrease continuously, which is characteristic of the dynamics near a Hopf bifurcation. The Bogdanov-Takens-cusp theory predicts not only the leak-induced bifurcation structures near the onset of APs, but also the Hopf bifurcation that terminates periodic spiking for high input-currents (Figs. 2A and S1, S4, and S6).
(D) f-I-curves for another DNLL cell (cf. Fig. 4A) that showed a transition in neuronal excitability and an enlargement of the region of bistability with increasing leak (cf. theory in Figs. 1-3, S4, and S6). Immediately after the switch (+5 nS), the region of bistability might be difficult to detect due its smallness.
(E) Width ΔI_{e} of the region of bistability for all intrinsically class-II DNLL cells in Fig. 4F that showed bistability. ΔI_{e} systematically increases with leak as predicted by theory (cf. Fig. 3B, S4, and S6). A subtraction in leak conductance in the cells that showed bistability led to onset spiking frequencies near the detection threshold for class-I neuronal excitability (Fig. 4F). The neuron in Fig. 4F that switched to class-I is colored brown.
(F,G) Latency from stimulus onset to the first action potential for (F) the intrinsically class-I and (G) class-II DNLL neurons in Fig. 4B and F, respectively. Increasing the leak conductance strongly decreased the time to the first spike, consistent with a transition form class-I to II neuronal excitability [8, 9, 10]. The neuron in Fig. 4F for which we observed a switch to class-I is colored red.
(H) Onset spiking frequency f_0 for intrinsically class-II CA3 pyramidal neurons for different values of externally added and subtracted leak. Neuronal dynamics in all cases became unstable for strongly negative external leak conductances.
(I) Width ΔI_{e} of the region of bistability for the and class-II CA3 cells. The increase in ΔI_e is predicted in Fig. 3 from the Bogdanov-Takens-cusp organization of leak-induced excitability transitions.
(J,K) Intrinsic measured leak vs. spike onset frequency is positively correlated in both DNLL (J) and CA3 (K) neurons. r is the correlation coefficient, ρ Spearmans rank order correlation coefficient with p the likelihood that the null hypothesis of zero correlation holds (p-value).

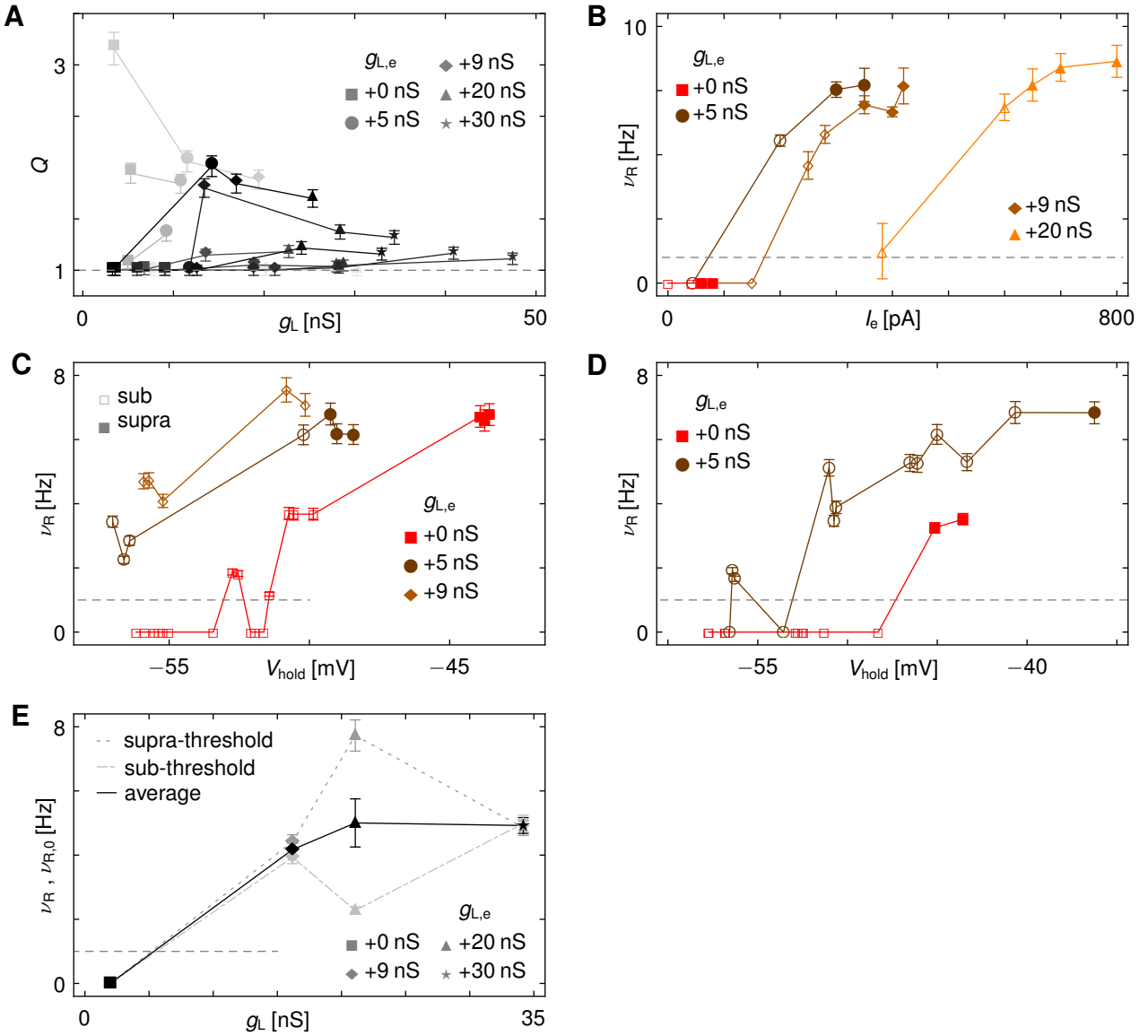

Supplementary Figure S8:
Leak-induced transition from integration to resonance in CA3 and DNLL neurons.
(A) Q factor $Q = |Z(\nu_{R,0})/Z(0)|$ for the resonances of CA3 pyramidal neurons shown in Fig. 5I as a function of the measured leak conductance g_L for different externally applied leak conductances $g_{L,e}$. An increase in leak conductance induced resonances in $n = 6/7$ non-resonant neurons, and it increased the resonance frequency in $n = 3/3$ neurons that were intrinsically resonant. Both increasing and decreasing Q values were observed. Linear theory predicts a monotonic increase (Fig. S3B).
(B) Dependence of the resonance frequency ν_R on the externally applied current I_e and the external leak conductance $g_{L,e}$ for the neuron shown in Fig. 5G,H. Open (solid) symbols indicate non-spiking (spiking) responses. For increasing g_L the resonance curves are shifted towards higher I_e and υ_R increases. Corresponding theory is shown in the main manuscript, Fig. 3B.
(C,D) Resonance frequency ν_R as a function of the holding potential V_{hold} for different values of the external leak conductance $g_{L,e}$ for two CA3 cells. The model predictions are in Figs. S3. The resonance frequencies generally increase with increasing membrane potential for all cells ($n = 12$). For an external leak conductance of +0 nS in (C) and +5 nS in (D), an initial resonance disappears before reappearing again as V_{hold} is increased. We observe such non-monotonic behavior in $n = 5/12$ cells. The non-monotonicity is consistent with the structure of leak induced resonance transitions organized by a Bogdanov-Takesn-cusp point (Figs. 2, S4 and S6). The range of leak conductances that lead to a non-monotonic relationship between ν_R and V_{hold} depends on the underlying active conductances (Figs. 2, S3, S4 and S6).
(E) Leak-induced resonance for the DNLL neuron in Fig. 4 in the main manuscript which parallels the leak-induced neuronal-excitability transition observed in Fig. 4A-D. CA3 neurons show the same behavior (Fig. 5).

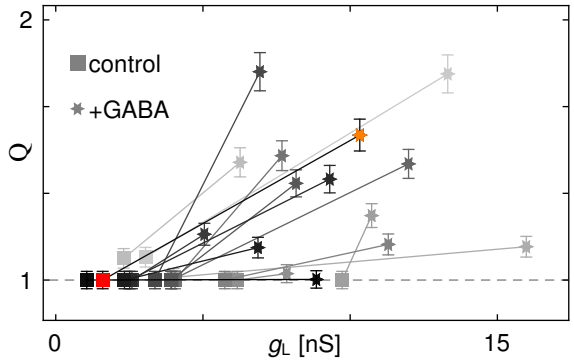

Supplementary Figure S9:
GABA-induced resonance in CA3 neurons.
Q factors $Q = |Z(\nu_0)/Z(0)|$ for the resonances in Fig. 6F show a systematic increase upon application of GABA, as predicted by theory (Fig. S3B). Colored dots represent neuron shown in Fig. 6D,E

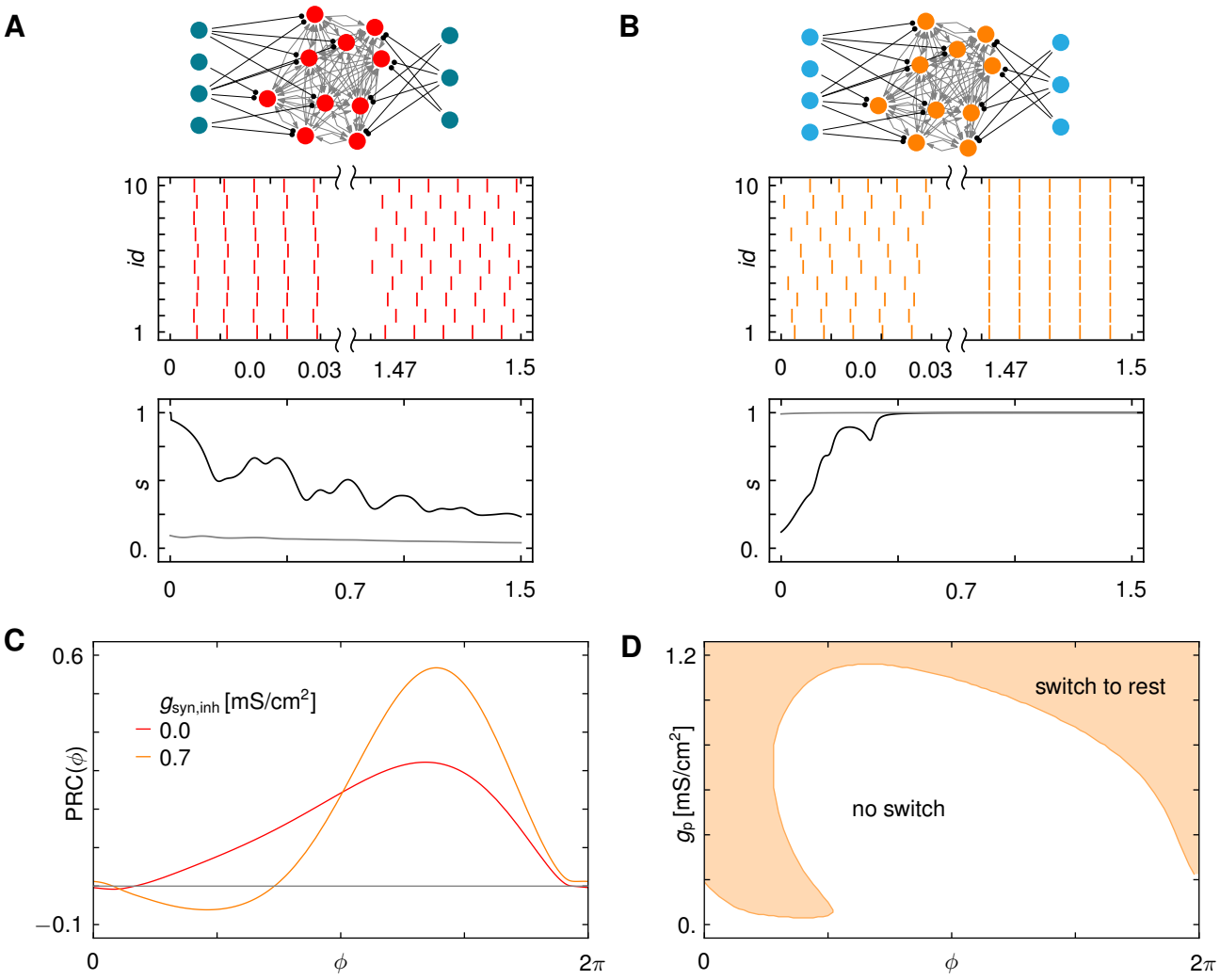

Supplementary Figure S10:
Leak-controlled synchronization, phase response and bistable switching.
(A) Network (top) of $N = 10$ excitatory Wang-Buzsáki neurons (red) receiving synapses from two groups of inhibitory neurons. For silent inhibitory neurons (dark turquoise), the excitatory neurons are class-I (red) and desynchronize. For initial conditions close to the synchronized state the neurons desynchronize (raster plot, middle) and the vector strength s decreases from 1 (bottom, black line) towards asynchronous state (gray line).
(B) Activation of all inhibitory neurons (top, light turquoise) switches all excitatory neurons to class-II (top, orange) which synchronize (raster plot, middle). Vector strength s for random initial conditions (bottom, black line) increases towards the synchronous state (gray line).
(C) Phase response curve PRC(ϕ) for the periodically spiking Wang-Buzsáki neurons in Fig. 7A-C with and without activation of a inhibitory conductance $g_{\mathrm{syn,inh}}$. A positive (negative) phase response $\mathrm{PRC}(\phi) > 0$ ($\mathrm{PRC}(\phi) < 0$) indicates that the next spike is advanced (delayed) due to small excitatory input at phase ϕ in the spiking cycle. A region with significant phase delay just after the spike ($\phi = 0$) is visible for the neuron with class-II excitability ($g_{\mathrm{syn,inh}} = 0.7\,\mathrm{mS/cm^2}$) and absent for class-I excitability ($g_{\mathrm{syn,inh}} = 0.0\,\mathrm{mS/cm^2}$). Weakly coupled tonically firing neurons with a negative PRC just after spiking synchronize [11], explaining the results in Fig. 7.
(D) Thresholds for bistable switching in the Wang-Buzsáki neurons. An isolated tonically firing neuron with period $T \approx 10\,\mathrm{ms}$ received the average shunting inhibition as in Fig. 7C and an additional excitatory synaptic current of the form $I_{\mathrm{syn,ex}}(t) = \Theta(t - t_0)\, g_{\mathrm{p}} \exp(-(t - t_0)/\tau_{\mathrm{d}})\,(V_{\mathrm{syn},ex} - V(t))$ with amplitude g_{p} and time delay $t_0 = \phi T/2\pi$. Here $t_0 = \phi = 0$ was chosen to mark the upward crossing of $-20\,\mathrm{mV}$ in the potential. In the shaded region, the excitatory pulse was able to trigger a switch from spiking to resting dynamics. Switching is possible for smaller inputs near the action potential ($\phi = 0$). The synchronization of the class-II neurons observed in Fig. 7C thus facilitates switching to the resting state via two effects: First, an increase in total synaptic pulse strength (i.e. g_{p}) as more neurons start to fire simultaneously and, second, by shifting the phase at which synaptic pulses are received towards $\phi = 0$ and thereby lowering the switching threshold. Together these two effects limit the number of synchronously firing neurons in the bistable region induced by shunting inhibition.

2 Organization of Neuronal Excitability Transitions

In this section we mathematically analyze transitions in neuronal excitability using multiple bifurcation theory. A focal or elliptic BTC point creates a three dimensional bifurcation structure in its neighborhood (its unfolding) as shown in Fig. 2C [1]. This unfolding provides a unified picture for all the theoretically and experimentally observed transition phenomena. In particular, the bifurcation diagrams with parameters spanned by the applied external current I_e and the leak conductance g_L (Figs. 1, 2, S1, S2, S4, S6) are two-dimensional slices of the three parameter unfolded bifurcation diagrams of the BTC points (Figs. 2, S1, S2) when the capacitance c_m is included as a third parameter. Further, other two-dimensional bifurcation diagrams obtained when altering the properties of the AP generating currents also represent such slices (Figs. S5). The co-occurrence of transitions in the f-I-curve, the creation of a region of bistability, as well as the structure of membrane resonance is thus inherently linked to the existence of a BTC point.

We here prove that class-I conductance-based neuron models have a co-dimension three Bogdanov-Takens-cusp (BTC) bifurcation point [1] in (I_e,g_L, c_m)-parameter space. We give precise conditions for the model that ensure the BTC point will be of either the focus or elliptic subtype [1]; furthermore, we show that these conditions for the sub-types are fulfilled in a large class of non-bursting neuron models. We conclude that leak-induced transitions in neuronal excitability are generically organized by BTC points.

To study the impact of leak currents onto the neuronal excitability class we consider general conductance-based neuron models of the form

$$\begin{aligned} c_\mathrm{m}\frac{d}{dt}V &= I_\mathrm{e} + g_\mathrm{L}\left(V_\mathrm{L} - V\right) + I_\mathrm{ion}\left(V,a\right) \\ \frac{d}{dt}a_j &= \frac{1}{\tau_j\left(V\right)}\left(a_{\infty,j}\left(V\right) - a_j\right) \end{aligned} \tag{S.1}$$

where V is the trans-membrane potential, c_m the capacitance, I_e the external input current, g_L and V_L the conductance and reversal potential of the leak current. The active ion currents are given by

$$I_\mathrm{ion}\left(V,a\right) = \sum_k g_k a_{i_{k,1}}^{l_{k,1}} \ldots a_{i_{k,p_k}}^{l_{k,p_k}} a_{\infty,j_{k,1}}^{m_{k,1}} \ldots a_{\infty,j_{k,q_k}}^{m_{k,q_k}} \left(V_k - V\right) \tag{S.2}$$

and depend on the maximal conductances g_k, reversal potentials V_j and activation variables $a = \left(a_2, a_2, \ldots, a_N\right)^T$ with steady state activations $a_{\infty,j}$ and time constants τ_j. Note that (S.1) also covers neuron models for which certain fast activation variables have been replaced by their steady state value $a_{\infty,j}\left(V\right)$.

We impose the following mathematical restrictions: (i) all conductances g_k in (S.2) are positive; (ii) the steady state activations are bounded, non-negative, monotonic, twice differentiable C^3 functions of V that become sufficiently flat in the limits $V \to \pm\infty$. In particular, we demand

$$\lim_{V\to\pm\infty} V\partial_V a_{j,\infty}\left(V\right) = 0. \tag{S.3}$$

By rescaling the activation functions they may be assumed without loss of generality to be normalized as

$$0 \leq a_{j,\infty}\left(V\right) \leq 1 \text{ for all } V \in \mathbb{R}. \tag{S.4}$$

Hodgkin classified neuronal excitability by the dependence of the firing rate f of a neuron on the input current I_e [12]: class-I has continuous f-I-curves while in class-II neurons spiking cannot be sustained below a certain non-zero frequency. A continuous f-I-curve implies periodic spiking solutions whose period becomes infinitely long as the input current I_e approaches the threshold current. In other words, by tuning I_e the time evolution in some part of the phase space can be made arbitrarily slow. Dynamical mechanisms that can lead to such divergences include the saddle-node on limit cycle as well as the homoclinic bifurcation (cf. Figs. 1 and S1). In neuron models, the membrane potential feeds back on itself: In class-I neurons where the critical current is reached a small membrane potential increase leads to a further increase in inward currents, which increase the membrane potential, causing more input current to flow. If this feedback can be made arbitrarily slow by approaching the threshold, the time to the next AP can be arbitrarily long. If the membrane potential evolves very slowly, the activation variables will have relaxed towards their steady-state values. Defining the steady steady-state I-V-curve as

$$I_\infty\left(V\right) = I_\mathrm{e} + g_\mathrm{L}\left(V_\mathrm{L} - V\right) + I_{\mathrm{ion},\infty}\left(V\right) \tag{S.5}$$

where

$$I_{\mathrm{ion},\infty}\left(V\right) = I_\mathrm{ion}\left(V, a_\infty\left(V\right)\right)$$

a positive feed back on arbitrarily slow times scales can be achieved if

$$\frac{d}{dV}I_\infty\left(V^+\right) > 0 \tag{S.6}$$

for some $V^+ \in \mathbb{R}$. We here define class-I neuronal dynamics by arbitrarily slow spiking generated by such a positive feedback mechanism. Thus, for class-I dynamics, a necessary (but not necessarily sufficient) condition is that there exists some V^+ for which (S.6) holds.

By using a combination of a center-manifold and normal form reduction [13, 14] together with multiple bifurcation theory [15, 16] we prove the following result:

Theorem 1. *Every conductance-based class-I neuron of the form (S.1) has a Bogdanov-Takens-Cusp point in the $(I_\mathrm{e}, g_\mathrm{L}, c_\mathrm{m})$-parameter space.*

Proof. There are two main features of Eq. (S.1) that facilitate our analytical treatment: First, the bifurcation parameters I_e, g_L, and c_m, are general parameters that appear in the vector fields of all conductance-based neuron models, with I_e and g_L appearing as coefficients of the constant and first order terms in V only. Second, the dynamics of the gating variables are coupled solely through the membrane potential V.

To simplify the notation, we introduce new parameters

$$b = \frac{1}{c_\mathrm{m}}, \quad I = \frac{I_\mathrm{e} + g_\mathrm{L} V_\mathrm{L}}{c_\mathrm{m}}, \quad \text{and} \quad g_\mathrm{l} = \frac{g_\mathrm{L}}{c_\mathrm{m}} \tag{S.7}$$

and rewrite the model (S.1) as

$$\frac{d}{dt}x = \frac{d}{dt}\begin{pmatrix} V \\ a \end{pmatrix} = \begin{pmatrix} I - g_\mathrm{l} V + b I_\mathrm{ion}(V,a) \\ \tau^{-1}(a_\infty - a) \end{pmatrix} = \begin{pmatrix} f_V(V,a) \\ f_a(V,a) \end{pmatrix} = f(V,a) = f(x) \tag{S.8}$$

where we set

$$\tau = \mathrm{diag}(\tau_2, \ldots, \tau_N), \quad a_\infty(V) = (a_{2,\infty}(V), \ldots, a_{N,\infty}(V))^T$$

We further use a notation in which multiplication of two vectors x and y is to be understood as their scalar product, i.e. $xy = \sum_i x_i y_i$ and denote the transpose of x by x^T. Partial derivatives ∂_a are understood as taking the derivative in each component of the a_i and thus applied to a scalar (a $N-1$ dimensional vector) the result is a $N-1$ dimensional vector (a $(N-1)\times(N-1)$ dimensional matrix). Further we use the short hand notations $\partial_{V,a} = \partial_V \partial_a$, $\partial_{V,V,a} = \partial_V^2 \partial_a$ etc.

We will show that one can always adjust the three parameters $\kappa = (I, g_\mathrm{l}, b)$ and the state vector x such that the system is at a co-dimension three BTC point. We denote this fixed point by $x_\mathrm{BTC} = x_0 = (V_0, a_{j,0})$ and the parameter values by $\kappa_\mathrm{BTC} = \kappa_0 = (I_0, g_{\mathrm{l},0}, b_0)$. The construction of the proof is as follows: $a_{j,0}$ and κ_0 can be expressed as functions of V_0 alone to satisfy $N+2$ out of the $N+3$ constraints for a codimension-3 BTC bifurcation. The last constraint reduces to an equation for V_0 that is independent of the parameter set κ_0 and can be shown to have a solution. We now proceed step by step.

A BTC point is a fixed point and thus, assuming the steady state voltage is given by V_0, setting the right hand side of (S.8) to zero the fixed point values $a_{j,0}$ for the activation variables are uniquely determined by

$$a_{j,0} = a_{j,\infty}(V_0) \tag{S.9}$$

Instead of solving for V_0 to satisfy the remaining fixed point equation obtained from (S.8) we use the observation that this equation can uniquely be solved for the parameter I_0 given x_0 and the parameters $g_{\mathrm{l},0}$ and b_0. We obtain

$$I_0 = -g_{\mathrm{l},0} V_0 - b_0 I_\mathrm{ion}(V_0, a_\infty(V_0)) \tag{S.10}$$

Besides being a fixed point, an ordinary Bogdanov-Takens (BT) point [17, 18] is characterized by a zero eigenvalue of algebraic multiplicity two and geometric multiplicity one, i.e. by a nilpotent Jacobian in the reduced dynamical system within a center-manifold. The Jacobian of (S.8) is given by

$$Df = \begin{pmatrix} \partial_V f_V & \partial_{a_2} f_V & \cdots & \partial_{a_N} f_V \\ \partial_V f_{a_2} & -\frac{1}{\tau_2} & & 0 \\ \vdots & & \ddots & \\ \partial_V f_{a_N} & 0 & & -\frac{1}{\tau_N} \end{pmatrix} = \begin{pmatrix} \partial_V f_V & \partial_a f_V^T \\ \partial_V f_a & -\tau^{-1} \end{pmatrix} \tag{S.11}$$

For a BT point at x_0 we therefore must demand the existence of four generalized eigenvectors q_0, q_1, p_0, p_1 of $A = Df|_{x_0}$, the Jacobian at x_0, such that

$$Aq_1 = q_0, \quad Dfq_0 = 0, \quad A^T p_0 = p_1, \quad A^T p_1 = 0, \quad p_i^T q_j = \delta_{ij}. \tag{S.12}$$

We now employ the fact that the dynamics of the activation variables a_j in a conductance based neuron model only couple via the membrane potential V. This is reflected in the special structure of Df, Eq. (S.11), having a block diagonal matrix on the lower right. Writing $q_j = (q_{j,1}, \ldots, q_{j,N})$ and $p_j = (p_{j,1}, \ldots, p_{j,N})$ for $i \in \{0,1\}$,

we can thus solve the equations (S.12) using (S.11) for all components $p_{j,i}$ and $q_{j,i}$ with $i \geq 2$ to obtain the q_j and p_j in the form

$$\begin{aligned} q_0 &= q_{0,1} \begin{pmatrix} 1 \\ \tau \partial_V f_a \end{pmatrix} & p_1 &= p_{1,1} \begin{pmatrix} 1 \\ \tau \partial_a f_V \end{pmatrix} \\ q_1 &= \begin{pmatrix} q_{1,1} \\ (q_{1,1} - q_{0,1}\tau)\, \tau \partial_V f_a \end{pmatrix} & p_0 &= \begin{pmatrix} p_{0,1} \\ (p_{0,1} - p_{1,1}\tau)\, \tau \partial_a f_V \end{pmatrix} \end{aligned} \tag{S.13}$$

The remaining equations for the first components with $i = 1$ then become

$$\begin{aligned} q_{0,1} \left(\partial_V f_V + \partial_a f_V \tau \partial_V f_a\right) &= 0 \\ q_{1,1} \left(\partial_V f_V + \partial_a f_V \tau \partial_V f_a\right) - q_{0,1} \left(1 + \partial_a f_V \tau^2 \partial_V f_a\right) &= 0 \\ p_{1,1} \left(\partial_V f_V + \partial_V f_a \tau \partial_a f_V\right) &= 0 \\ p_{0,1} \left(\partial_V f_V + \partial_a f_V \tau \partial_V f_a\right) - p_{1,1} \left(1 + \partial_a f_V \tau^2 \partial_V f_a\right) &= 0 \end{aligned}$$

As the generalized eigenvectors must be non-zero, we have $q_{0,1} \neq 0 \neq p_{1,1}$ and the solvability of the above system yields

$$\partial_V f_V + \partial_a f_V \tau \partial_V f_a = 0 \tag{S.14}$$

$$1 + \partial_a f_V \tau^2 \partial_V f_a = 0 \tag{S.15}$$

These equations render the fixed point x_0 to be an ordinary Bogdanov-Takens point. Using (S.8) we have

$$\partial_V f_a = \tau^{-1} \partial_V a_\infty - \tau^{-2} \left(\partial_V \tau\right) \left(a_\infty - a\right) \quad \text{and thus} \quad \partial_V f_a|_{x_0} = \tau^{-1} \partial_V a_\infty \big|_{V_0}$$

as $a = a_\infty$ at x_0 via the fixed point condition (S.9). Hence, the first condition (S.14) is equivalent to

$$\frac{d}{dV} I_\infty|_{x_0} = 0 \tag{S.16}$$

Note that this equation is also equivalent to the condition that the determinant at x_0 given by

$$\det\left(Df\right)|_{x_0} = \frac{(-1)^{N-1}}{\prod_j \tau_j} \left(\partial_V f_V + \left(\partial_V a_\infty\right) \partial_a f_V\right)\Big|_{x_0} = \frac{(-1)^{N-1}}{\prod_j \tau_j} \frac{d}{dV} I_\infty \Big|_{x_0} \tag{S.17}$$

evaluates to zero indicating the position of a fold point in general. The fold condition (S.16) is a linear equation in the two parameters g_l and b and can be solved uniquely for g_l to give

$$g_{l,0} = b_0 \frac{d}{dV} I_{\text{ion}}\left(V, a_\infty\left(V\right)\right)\Big|_{V_0} = b_0 \frac{d}{dV} I_{\text{ion},\infty}\left(V\right)\Big|_{V_0} \tag{S.18}$$

The next step is to solve the second BT point condition (S.15) for the parameter b which gives

$$b_0^{-1} = -\partial_a I_{\text{ion}} \tau \partial_V a_\infty|_{V_0} \tag{S.19}$$

For a two-dimensional system, this condition becomes $\operatorname{tr}\left(Df\right)|_{x_0} = 0$ and together with (S.17) this again shows that these are the conditions for an ordinary BT point.

As a next step, we calculate the equation that forces the BT point to be degenerate, i.e. a BTC point. The results in [17, 18] imply that in any two dimensional center manifold with properly chosen coordinates (w_0, w_1) centered at a BT fixed point, the the system can be written in the following form

$$\begin{aligned} \frac{d}{dt} w_0 &= w_1 \\ \frac{d}{dt} w_1 &= \alpha_2 w_0^2 + \beta_2 w_0 w_1 + \mathcal{O}\left(\left\|(w_0, w_1)\right\|^3\right) \end{aligned} \tag{S.20}$$

with constant coefficients α_2 and β_2 that depend on the details of the original model. A BT point is degenerate if either $\alpha_2 \neq 0$, $\beta_2 = 0$ or $\alpha_2 = 0$, $\beta_2 \neq 0$ [1, 19, 20]. We consider the second case, which encompasses the focus and elliptic BTC points of relevance to leak-induced transitions. We now show that we can tune the fixed point value V_0 such that $\alpha_2 = 0$.

The normal form coefficient α_2 can be directly calculated using center-manifold theory and imposing the Fredholm solvability conditions [14]. This yields an expression for α_2 in terms of the generalized eigenvectors q_0 and p_1, (S.12) as

$$\alpha_2 = \frac{1}{2} p_1 D^2 f\left(x_0\right)\left(q_0, q_0\right), \tag{S.21}$$

where $D^2 f(x)(\cdot,\cdot)$ is the Hessian quadratic form of the vector field f at x . Using the expressions (S.13) for the generalized eigenvectors we obtain

$$\begin{aligned}\frac{1}{q_{0,1}^2} D^2 f_V(x_0)(q_0,q_0) &= \partial_{V,V} f_V + 2(\partial_{V,a} f_V)\tau\partial_V f_a + (\partial_V f_a)\tau(\partial_{a,a} f_V)\tau\partial_V f_a\big|_{x_0} \\ \frac{1}{q_{0,1}^2} D^2 f_a(x_0)(q_0,q_0) &= \partial_{V,V} f_a + 2(\partial_{V,a} f_a)\tau\partial_V f_a + \partial_{a,a} f_a(\tau\partial_V f_a, \tau\partial_V f_a)\big|_{x_0} \\ &= \partial_{V,V} f_a + \tau^{-2}(\partial_V \tau)(\tau\partial_V f_a)\big|_{x_0}\end{aligned}$$

where in the second equation we used $\partial_a f_a = -\tau^{-1}$ and $\partial_{a,a} f_a = 0$. Thus

$$\begin{aligned}\frac{2}{p_{1,1} q_{0,1}^2}\alpha_2 &= \partial_{V,V} f_V + 2(\partial_{a,V} f_V)\tau\partial_V f_a + (\partial_V f_a)\tau(\partial_{a,a} f_V)\tau\partial_V f_a \\ &\quad + (\partial_a f_V)\tau\partial_{V,V} f_a + 2\tau(\partial_a f_V)\tau^{-2}(\partial_V\tau)\tau\partial_V f_a\big|_{x_0}\end{aligned}$$

Using

$$\partial_{V,V} f_a\big|_{x_0} = \tau^{-1}\partial_{V,V} a_\infty - 2\tau^{-2}(\partial_V\tau)\partial_V a_\infty\big|_{x_0}$$

we obtain

$$\begin{aligned}\frac{2}{p_{1,1} q_{0,1}^2}\alpha_2 &= \partial_{V,V} f_V + 2(\partial_{V,a} f_V)\partial_V a_\infty + (\partial_V a_\infty)(\partial_{a,a} f_V)\partial_V a_\infty + (\partial_a f_V)\partial_{V,V} a_\infty\big|_{x_0} \\ &= \frac{d^2}{dV^2} I_\infty\Big|_{x_0}\end{aligned}$$

The degeneracy condition for the BT point thus becomes

$$\frac{d^2}{dV^2} I_\infty\Big|_{x_0} = 0. \tag{S.22}$$

Now we use the second ingredient, namely that the I and g_l are coefficients of the constant and linear part of the vector field f so that $\frac{d^2}{dV^2} I_\infty$ does not depend on I and g_l. It is further proportional to $b \neq 0$, so that the condition can be solved for V_0 independently of the choice of the parameters (I, g_L, b).

To show the existence of a solution to (S.22) we use the precondition that the neuron has class-I excitability, i.e. the neuron satisfies (S.6). Observe that I_∞ has the form $I_\infty(V) = q(V) - p(V)V$, for which $q(V)$ and $p(V)$ are pure polynomials in the variables $a_{j,\infty}(V)$. As all maximal conductances and activation variables are positive, we have $p(V) \geq g_\mathrm{l} > 0$ and thus using (S.3) we obtain

$$\lim_{V\to\pm\infty} \frac{d}{dV} I_\infty(V) \leq -g_\mathrm{l}. \tag{S.23}$$

Combining equations (S.6) and (S.23) it follows that $\frac{d}{dV} I_\infty$ must have at least one local maximum and hence there is a $V_0 \in \mathbb{R}$ such that $\frac{d^2}{dV^2} I_\infty(V)\Big|_{V=V_0} = 0$. Finally, given V_0 that solves the degeneracy condition (S.22) the equations (S.10), (S.18) and (S.19) show that there exists a parameter set $(I_0, g_{l,0}, b_0)$ such that x_0 is a BTC point. □

This shows the existence of a BTC point in all class-I conductance based neuron models. The following lemma provides a condition for the neuron model to ensure that the BTC point lies in a bio-physically plausible parameter regime.

Lemma 2. *For a class-I conductance based neuron model of the form (S.1) the BTC point at $x_0 = (V_0, a_0)$ and $\kappa_0 = (I_0, g_{l,0}, b_0)$ is bio-physically permissible, i.e. we have*

$$g_{\mathrm{L},0} = \frac{g_{\mathrm{l},0}}{b_0} > 0 \quad \textit{and} \quad c_{\mathrm{m},0} = \frac{1}{b_0} > 0$$

if

$$\partial_a I_\mathrm{ion}\tau\partial_V a_\infty\big|_{x_0} < 0 \tag{S.24}$$

holds.

Proof. In the proof of the Theorem above we showed that $\frac{d}{dV}I_\infty$ has at least one local maximum. Combining (S.6) with (S.18) and (S.19) shows that choosing V_0 at such maximum we have

$$\mathrm{sign}\left(\mathrm{g_{l,0}}\right) = \mathrm{sign}\left(b_0\right) = -\mathrm{sign}\left(\partial_{\mathrm{a}}\mathrm{I_{ion}}\tau\partial_{\mathrm{V}}\mathrm{a}_\infty|_{\mathrm{x}_0}\right).$$

The condition (S.24) then implies that

$$\mathrm{sign}\left(g_{\mathrm{L},0}\right) = \mathrm{sign}\left(g_{\mathrm{l},0}\right)\mathrm{sign}\left(b_0\right) = 1$$

and

$$\mathrm{sign}\left(c_{\mathrm{m},0}\right) = \mathrm{sign}\left(b_0\right) = 1$$

□

We next calculate some useful expressions occurring frequently in the calculations that follow.

Lemma 3. *For a class-I conductance based neuron model of the form (S.1) at a BTC point $x_0 = (V_0, a_0)$ and $\kappa_0 = (I_0, g_{l,0}, b_0)$ the following identities hold*

$$\begin{aligned}
a_\infty\left(V_0\right) &= a_0 \\
\frac{d}{dV}a_\infty\left(V_0\right) &= \tau\partial_V f_a|_{x_0} \\
\frac{d^2}{d^2V}a_\infty\left(V_0\right) &= \tau\partial_{V,V}f_a + 2\tau^2\partial_{V,a}f_a\partial_V f_a\big|_{x_0} \\
\frac{d^3}{d^3V}a_\infty\left(V_0\right) &= \tau\partial_{V,V,V}f_a + 3\tau^2\partial_{V,a}f_a\partial_{V,V}f_a + 3\tau^2\partial_{V,V,a}f_a\partial_V f_a + 6\tau^3\left(\partial_{V,a}f_a\right)^2\partial_V f_a\Big|_{x_0}
\end{aligned}$$

and

$$\begin{aligned}
\tau\left(V_0\right) &= -\left(\partial_a f_a\right)^{-1}\Big|_{x_0} \\
\frac{d}{dV}\tau\left(V_0\right) &= \tau^2\partial_{a,V}f_a\big|_{x_0} \\
\frac{d^2}{dV^2}\tau\left(V_0\right) &= \tau^2\partial_{a,V,V}f_a + 2\tau^3\left(\partial_{V,a}f_a\right)^2\Big|_{x_0}
\end{aligned}$$

further we have

$$\begin{aligned}
I_\infty\left(V_0\right) &= f_V|_{x_0} = f_V\left(V_0, a_\infty\left(V_0\right)\right) = 0 \\
\frac{d}{dV}I_\infty\left(V_0\right) &= \partial_V f_V + \left(\partial_a f_V\right)\tau\partial_V f_a|_{x_0} = 0 \\
\frac{d^2}{dV^2}I_\infty\left(V_0\right) &= \partial_{V,V}f_V + 2\left(\partial_{V,a}f_V\right)\tau\partial_V f_a + \partial_V f_a\tau\left(\partial_{a,a}f_V\right)\tau\partial_V f_a \\
&\quad + \left(\partial_a f_V\right)\tau\left(\partial_{V,V}f_a + 2\tau\left(\partial_{V,a}f_a\right)\partial_V f_a\right)|_{x_0} \\
&= 0 \\
\frac{d^3}{dV^3}I_\infty\left(V_0\right) &= \partial_{V,V,V}f_V + \partial_{a,a,a}f_V\left(\tau\partial_V f_a, \tau\partial_V f_a, \tau\partial_V f_a\right) + \left(\partial_a f_v\right)\tau\partial_{V,V,V}f_a + 3\left(\partial_{V,a}f_V\right)\tau\partial_{V,V}f_a \\
&\quad + 3\left(\partial_{V,V,a}f_V\right)\tau\partial_V f_a + 3\left(\partial_a f_V\right)\tau^2\left(\partial_{V,a}f_a\right)\partial_{V,V}f_a + 3\left(\partial_a f_V\right)\tau^2\left(\partial_{V,V,a}f_a\right)\partial_V f_a \\
&\quad + 3\left(\partial_a f_V\right)\tau\left(\partial_{a,a}f_V\right)\tau\partial_{V,V}f_a + 3\left(\partial_a f_V\right)\tau\left(\partial_{V,a,a}f_V\right)\tau\partial_V f_a + 6\left(\partial_a f_V\right)\tau^3\left(\partial_{V,a}f_a\right)^2\partial_V f_a \\
&\quad + 6\left(\partial_a f_{V,V}\right)\tau^2\left(\partial_{V,a}f_a\right)\partial_V f_a + 6\left(\partial_a f_V\right)\tau\left(\partial_{a,a}f_V\right)\tau^2\left(\partial_{V,a}f_a\right)\partial_V f_a\big|_{x_0} \\
&< 0
\end{aligned}$$

Proof. The first two sets of identities follow from lengthy but direct algebraic computation using the structure of the conductance-based neuron model, such as $\partial_{a,a}f_a = 0$ and the fact that $\partial_a f_a$ is a diagonal matrix, together with the properties of the BTC point such as $a_0 = a_\infty\left(V_0\right)$ and e.g. $\partial_V f_a|_{x_0} = \tau^{-1}\left(\partial_V a_\infty - \tau^{-1}\partial_V\tau\left(a_\infty - a\right)\right)\big|_{V_0} = \tau^{-1}\partial_V a_\infty\big|_{V_0}$. The equations for the expressions $\frac{d^n}{dV^n}I_\infty\left(V_0\right)$ then follow directly by applying the above identities for a_∞ and τ and the BTC conditions. The inequality

$$\frac{d^3}{dV^3}I_\infty\left(V_0\right) < 0 \tag{S.25}$$

follows from the choice of V_0 as a local maximum of $\frac{d}{dV}I_\infty\left(V_0\right)$ in the proof of the Theorem above. □

We now consider the precise type of BTC points encountered in conductance-based neuron models. In the representation of the center manifold dynamics as in (S.20) we therefore also consider terms of higher order. For a system at a BTC bifurcation point with $\alpha_2 = 0$ there is a smooth coordinate change and time re-parametrization such that the reduced model dynamics in (S.20) on the center manifold take the form [1, 14]

$$\begin{aligned}\frac{d}{dt}u_0 &= u_1\\ \frac{d}{dt}u_1 &= \alpha_3 u_0^3 + \beta_2 u_0 u_1 + \gamma_3 u_0^2 u_1 + \mathcal{O}\left(\|(u_0,u_1)\|^5\right)\end{aligned}$$

If necessary a further coordinate change can be applied to assure that β_2 is positive. Now the precise values of α_3 and β_2 with $\alpha_3\beta_2 \neq 0$ determine the sub-type of the BTC point. In particular the point is of saddle type if $\alpha_3 > 0$. It is of elliptic type if $\alpha_3 < 0$ and $\beta_2^2 + 8\alpha_3 > 0$ and a focus if $\alpha_3 < 0$ and $\beta_2^2 + 8\alpha_3 < 0$. Note that the focus requires $\gamma_3 \neq 0$ and is stable if $\gamma_3 < 0$ [1, 14].

Proposition 4. *For a conductance-based neuron model of the form (S.1) with a BTC point at $x_0 = (V_0, a_0)$ and $\kappa_0 = (I_0, g_{l,0}, \alpha_0)$ the normal form coefficients α_2,β_2 and α_3 are given by*

$$\begin{aligned}\alpha_2 &= \frac{1}{2}p_{1,1}q_{0,1}^2\frac{d^2}{dV^2}I_\infty(V_0) = 0\\ \alpha_3 &= \frac{1}{6}p_{1,1}q_{0,1}^3\frac{d^3}{dV^3}I_\infty(V_0)\\ \beta_2 &= -p_{1,1}q_{0,1}^2\left[\partial_V\left(\left(\partial_a f_V\right)\tau^2\partial_V f_a\right) + \left(\partial_a f_V\right)\tau^3\left(\partial_{V,a} f_a\right)\partial_V f_a + \left(\partial_a f_V\right)\tau\left(\partial_{a,a} f_V\right)\tau^2\partial_V f_a\right]\Big|_{x_0}\\ &> 0\end{aligned}$$

where

$$p_{1,1}q_{0,1} = -\frac{1}{\left(\partial_a f_V\right)\tau^3\left(\partial_V f_a\right)}\Bigg|_{x_0} \qquad q_{0,1} = \pm\frac{1}{\sqrt{1+\left(\partial_a f_V\right)\tau^2\partial_a f_V}}\Bigg|_{x_0}$$

If furthermore

$$\partial_a I_{\text{ion}}\tau^3\partial_V a_\infty\big|_{x_0} < 0 \tag{S.26}$$

the BTC point is of focus or elliptic sub-type.

Proof. The normal form coefficients α_2, α_3 and β_2 can be calculated by imposing solvability conditions onto linear systems that arise in the combined calculation of the normal form reduction and center-manifold coordinates [14]. The resulting expression for α_2 is given above in (S.21), while the other coefficients are

$$\begin{aligned}\beta_2 &= p_0 D^2 f(x_0)(q_0,q_0) + p_1 D^2 f(x_0)(q_1,q_0)\\ \alpha_3 &= \frac{1}{6}p_1 D^3 f(x_0)(q_0,q_0,q_0) + \frac{1}{2}p_1 D^2 f(x_0)(h_{20},q_0)\end{aligned}$$

where

$$h_{20} = q_{0,1}^2\left(0, \frac{d^2}{dV^2}a_\infty(V_0)\right)$$

The scalars $p_{1,1}$ and $q_{0,1}$ can be calculated from the normalization conditions given in (S.12) and the additional normalization conditions $q_0 q_0 = 1$ and $q_0 p_1 = 0$. Then, by evaluating the expressions for the normal form coefficients and using the identities from the previous lemma we obtain the result after lengthy but straightforward algebra. □

Neuron Model	class	V_0 [mV]	I_0 [μA/cm^2]	$g_{\mathrm{L},0}$ [mS/cm^2]	$c_{\mathrm{m},0}$ [μF/cm^2]	β_2	α_3	BTC type
Morris and Lecar [3]	I	-11.90	175.62	5.53	42.69	0.011	-2.28×10^{-5}	focus
Wang and Buysaki [2]	I	-46.75	7.68	0.74	1.53	0.13	-2.73×10^{-3}	focus
Erisir et al. [4]	I	-39.34	15.24	0.83	5.88	0.021	-1.12×10^{-4}	focus
Rose and Hindmarsh [21]	I	-37.59	305.9	11.26	35.90	0.082	-1.85×10^{-3}	focus
Destexhe and Pare [22]	I	-47.29	9.77	0.32	407.5	0.0003	-1.71×10^{-7}	focus
Prescott et al. [23]	I	-36.27	19.95	0.85	19.80	0.0034	-1.67×10^{-5}	focus
Golomb et al. [24]	I	-50.57	1.35	0.14	1.16	0.029	-1.03×10^{-4}	focus
Acker et al. [25]	I	-82.34	-0.066	0.0016	0.15	0.031	-4.85×10^{-7}	elliptic
Ermentrout and Kopell [6]	I	-49.71	98.53	8.20	30.41	0.17	-2.43×10^{-3}	elliptic
Hodgkin and Huxley [26]	II	-18.08	-14.67	-0.28	-0.042	0.021	2.45×10^{-4}	saddle

Supplementary Table S1
Bogdanov-Takens-cusp bifurcation points in neuron models. For each conductance based neuron model the resting potential V_0 as well as the parameter $(I_0, g_{\mathrm{L},0}, c_{\mathrm{m},0})$ at the BTC point at $x_0 = (V_0, a_\infty(V_0))$ are listed together with the non-zero normal form coefficients. All intrinsic class-I neuron models have either a BTC bifurcation point of elliptic or focus sub-type. The focus type is prevalent for intrinsically class-I neurons, while a saddle type BTC is not encountered. Intrinsically class-II neurons are not subject to the Theorem. For instance, the Hodgkin-Huxley model is class-II; the BTC point in this case is found at negative $c_{\mathrm{m},0}$ and $g_{\mathrm{L},0}$, which are not bio-physically plausible ; moreover, the putative BTC point is of saddle type.

We used the Theorem and Proposition derived here to determine the BTC points and their sub-type in various conductance-based neuron models. The results in Table S1 show that intrinsically type I neurons are either of focus or elliptic sub-types. Both of these BTC points yield a common topology for the bifurcation diagrams in the in the $(I_{\mathrm{e}}, g_{\mathrm{L}})$-plane (Fig. S1). For the elliptic sub-type the full theory requires one to restrict the analysis to a bounded region in phase-space encircling the fixed points. This local restriction imposes additional border tangency bifurcations in the bifurcation diagram [1]. However, when taking into account the full phase space, we numerically observe that these border bifurcations give rise to global bifurcations that, in their sum, render the bifurcation diagram as shown in Fig. S1. This observation holds for both the unfolded normal form of the elliptic BTC as well as for all the class-I neurons models of elliptic type considered here. Thus, all class-I neurons show the same sequence of transitions in the f-Icurves, bistability and resonance organized by a focus or elliptic BTC bifurcation point.

More than one solution to eq. (S.22) can exist. For the neuron models studied above, we typically find two to five solutions. About half of the solutions correspond to minima of $\frac{d}{dV} I_\infty$ and imply that $g_{\mathrm{L},0}$ has the opposite sign of $c_{\mathrm{m},0}$; such parameters lead to unstable unbounded dynamics. Numerically we find that in all class-I neuron models considered, there is a single unique focus or elliptic BTC point among all solutions with biophysical permissible parameters. Moreover, the overall organization of the bifurcation diagrams in the $(I_{\mathrm{e}}, g_{\mathrm{L}})$-plane is as depicted in Fig. S1 or S2. The existence of other degenerate bifurcation points may alter the fine structure of the bifurcation diagram. For example, in the original Connor-Stevens model we observe that in the transition from class-I to class-II the $(I_{\mathrm{e}}, g_{\mathrm{L}})$-bifurcation diagram shows additional signatures of a nearby swallowtail bifurcation (cf. [16] for definition).

We had to demand class-I excitability in order to ensure the existence of a BTC point. For class-II neurons a BTC may still exist, however, one cannot exclude negative values of $g_{\mathrm{L},0}$ or a saddle BTC point with unbounded dynamics (cf. the Hodgkin-Huxley model in Table S1). Further, to define class-I excitability we used Eq. (S.6), i.e. the existence of a arbitrarily slow positive feedback in the voltage evolution. For planar dynamics (any system with only two dynamical variables), this is a natural consequence of the presence of a saddle-point. Indeed, one can show the following:

Lemma 5. *Suppose a conductance-based neuron model given by Eq. (S.1) has a continuous f-I-curve and can be mapped by a diffeomorphism onto a planar system while preserving the voltage variable $V(t)$. Then this model has a steady-state I-V-curve that satisfies (S.6), i.e. for some V^+ we have $\frac{d}{dV} I_\infty(V^+) > 0$.*

Proof. We briefly sketch the arguments here. The dynamics for the activation variables a are bounded by definition of the neuron model class Eq. (S.1). Set $V_{\max} = \max_j V_j$ and $V_{\min} = \min_j V_j$. For $V > \max\left(V_{\max}, \frac{I_{\mathrm{e}} + g_{\mathrm{L}} V_{\mathrm{L}}}{g_{\mathrm{L}}}\right)$ the total current $I_{\mathrm{tot}} = I_{\mathrm{e}} + g_{\mathrm{L}}(V_{\mathrm{L}} - V) + I_{\mathrm{ion}}(V, a)$ becomes negative while for $V < \min\left(V_{\min}, -\frac{I_{\mathrm{e}} + g_{\mathrm{L}} V_{\mathrm{L}}}{g_{\mathrm{L}}}\right)$, $I_{\mathrm{tot}} > 0$. Thus, the dynamics in V is bounded, too, so that overall dynamics is confined.

In two dimensions, a continuous f-I-curve can only arise via a saddle-node on limit cycle or a homoclinic bifurcation; the only two other generic one-parameter bifurcations that give rise to a stable limit cycle in two dimensions are Hopf and double limit cycle bifurcations, each of which generates a discontinuous f-I-curve,

cf. [16, 27]). Both, the SNLC and homoclinic bifurcations imply the existence of a saddle fixed-point. Now, for generic and bounded two dimensional dynamics Poincaré index theory dictates that a saddle-fixed point arises only when accompanied by two other fixed points (called nodes). The steady-state $I_\infty(V)$ must vanishes at these points. As the steady state variables a are uniquely determined by the steady state voltage at a fixed point, we conclude that $I_\infty(V)$ must have at least three zeros. Now as $\frac{d}{dV}I_\infty(V)$ is continuous and becomes negative in the limits $V \to \pm\infty$, the sign of $\frac{d}{dV}I_\infty(V)$ must alternate across the three fixed point solutions. In other words, there must be at least one solution for which $\frac{d}{dV}I_\infty(V^+) > 0$. Qualitatively speaking, the steady-state I-V-curve must "curve back" to yield three fixed point solutions of Eq. (S.1). □

To summarize, we here analytically showed the existence of BTC points in all conductance-based class-I neuron models, as supported by numerical simulations of different neuron models (Figs. 1-3, S3-S6, Table S1). We demonstrated that in class-I neurons the BTC point is either of focus or elliptic type. A BTC point of focus type implies the existence of three organizing centers of co-dimension two: an NSL a SNL and a DH bifurcation that regulate the transition of neuronal excitability from class-I (via a SNLC bifurcation) to class-II (via a DC bifurcation). The elliptic type guarantees a transition from SNLC to DC bifurcations, but does not specify the exact sequence of intermediate non-local bifurcations. Nonetheless, numerically calculated bifurcations diagrams for class-I neuron models with an elliptic type BTC point, show that the same transition structure from SNLC to DC via a homoclinic bifurcation occurs. Both, elliptic and focus BTC points organize leak-induced bistability and predict a BT bifurcation that controls the transition from sub-threshold to peri-threshold resonance. We conclude that excitability transitions in class-I neurons are generally organized by a BTC bifurcation of elliptic or focus type. The unfolding of the BTC bifurcation provides a unified explanation for all the experimentally observed co-occuring sub-transitions (Figs. 4-6, S7-S9).

3 Supplementary Methods

Experiments and Data Analysis

All experiments were done and all data analyzed as described in the main text. The latency from stimulus onset to the first spike was determined form the traces of the f-I-experiments, i.e. from the voltage response to injection of step currents of 1s duration with a fine current amplitude increase of fixed step size of 1-20 pA starting close to but below the threshold. The latency was then determined from the trace with lowest step current amplitude displaying at least one spike. Q-factors were determined form the fitted impedance curves via $Q = |Z(\nu_R)/Z(0)|$.

Neuron Models

Bifurcation diagrams for the neuron models were obtained as in the main text using the numerical continuation software AUTO [28] with HomCont [29]. Model dynamics were simulated in Wolfram's Mathematica 9. The conductance-based neuron models dynamics are given in (S.1). For voltage-dependent opening and closing rates $\alpha_a(V)$ and $\beta_a(V)$ of the activation variable a, the time constant is $\tau_a^{-1}(V) = \alpha_a(V) + \beta_a(V)$ and the steady state activation is given by $a_\infty(V) = \alpha_a(V)\tau_a(V)$. Phase response curves for the models were determined by solving the adjoint equation as described in [11]. Normal form coefficients were calculated according to the theorem and proposition proved above. Neuron models in Table S1 not listed below used equations and parameter as in the listed references.

The Wang-Buzsáki Neuron Model The Wang-Buzsáki neuron model [2] is defined by the equation

$$c_\mathrm{m}\frac{d}{dt}V = I_\mathrm{e} + I_\mathrm{syn} + g_\mathrm{L}(V_\mathrm{L} - V) + g_{Na}m_\infty^3 h(V_{Na} - V) + g_K n^4(V_K - V) \tag{S.1}$$

supplemented by the dynamics for the gating variables n and h as in (S.1). The rate constants are:

$$\begin{aligned}
\alpha_m(V) &= \frac{0.1(V+35)}{1-\exp(-0.1(V+35))} & \beta_m(V) &= 4.0\exp\left(-\frac{(V+60)}{18}\right)\\
\alpha_h(V) &= 0.07\exp\left(-\frac{(V+58)}{20}\right) & \beta_h(V) &= \frac{1.0}{1+\exp(-0.1(V+28))}\\
\alpha_n(V) &= \frac{0.01(V+34+b_\mathrm{n})}{1-\exp(-0.1(V+34+b_\mathrm{n}))} & \beta_n(V) &= 0.125\exp\left(-\frac{(V+44+b_\mathrm{n})}{80}\right) \quad .
\end{aligned} \tag{S.2}$$

Parameters are as in [2] with $c_\mathrm{s} = 1\,\frac{\mu\mathrm{F}}{\mathrm{cm}^2}$, $g_\mathrm{Na} = 35\,\frac{\mathrm{mS}}{\mathrm{cm}^2}$, $g_\mathrm{K} = 9\,\frac{\mathrm{mS}}{\mathrm{cm}^2}$, $g_\mathrm{L} = 0.1\,\frac{\mathrm{mS}}{\mathrm{cm}^2}$, $V_\mathrm{Na} = 35\,\mathrm{mV}$, $V_\mathrm{K} = -90\,\mathrm{mV}$ and $V_\mathrm{L} = -65\,\mathrm{mV}$. We introduced the parameter b_n that shifts the half-activation and time constants of the delayed rectifier along the direction of the membrane potential.

The Morris-Lecar Neuron Model The Morris-Lecar neuron model [3] is defined by

$$\begin{aligned} c_\mathrm{m}\frac{d}{dt}V &= I_\mathrm{e} + I_\mathrm{syn} + g_L\left(V_\mathrm{L} - V\right) + g_\mathrm{Na} m_\infty\left(V\right)\left(V_\mathrm{Na} - V\right) + g_\mathrm{K} n\left(V_\mathrm{K} - V\right) \\ \frac{d}{dt}n &= \frac{1}{\tau_w\left(V\right)}\left(n_\infty\left(V\right) - n\right) \end{aligned} \tag{S.3}$$

with activation variables evolving according

$$\begin{aligned} m_\infty\left(V\right) &= \frac{1}{2}\left(1 + \tanh\left(\frac{V - V_1}{V_2}\right)\right) \\ n\left(V\right) &= \frac{1}{2}\left(1 + \tanh\left(\frac{V - V_3}{V_4}\right)\right) \qquad \tau_n^{-1}\left(V\right) = \Phi^{-1}\cosh\left(\frac{V - V_3}{V_4}\right) \end{aligned} \tag{S.4}$$

with parameters from [8, 11] given by $c_\mathrm{m} = 20\,\frac{\mu\mathrm{F}}{\mathrm{cm}^2}$, $g_\mathrm{Na} = 4.0\,\frac{\mathrm{mS}}{\mathrm{cm}^2}$, $g_\mathrm{K} = 8.0\,\frac{\mathrm{mS}}{\mathrm{cm}^2}$, $g_\mathrm{L} = 2.0\,\frac{\mathrm{mS}}{\mathrm{cm}^2}$, $V_\mathrm{Na} = 120\,\mathrm{mV}$, $V_\mathrm{K} = -80.0\,\mathrm{mV}$,$V_\mathrm{L} = -60\,\mathrm{mV}$. Half-activation and slope of the activation curves are $V_1 = -1.2\,\mathrm{mV}$, $V_2 = 18\,\mathrm{mV}$, $V_3 = 12\,\mathrm{mV}$ and $V_4 = 17.4\,\mathrm{mV}$ and the temperature constant $\Phi^{-1} = 15$.

The Fast Spiking Neuron Model by Erisir et al. The fast spiking neuron model [4] is defined by

$$c_\mathrm{m}\frac{d}{dt}v = I_\mathrm{e} + I_\mathrm{syn} + g_\mathrm{L}\left(V_\mathrm{L} - V\right) + g_\mathrm{Na} m^3 h\left(V_\mathrm{Na} - V\right) + g_\mathrm{K} n^2\left(V_\mathrm{K} - V\right) \tag{S.5}$$

supplemented with the standard equations for the dynamics of the gating variables m, h and n with voltage dependent rates

$$\begin{aligned} \alpha_m\left(V\right) &= \frac{\left(40V + 3020\right)}{1 - \exp\left(-\left(V - 75.5\right)/13.5\right)} \qquad \beta_m\left(V\right) = 1.2262\exp\left(-\frac{V}{42.248}\right) \\ \alpha_h\left(V\right) &= 0.0035\exp\left(-\frac{v}{24.186}\right) \qquad \beta_h\left(V\right) = 0.017\frac{\left(51.25 + V\right)}{1 - \exp\left(-\left(51.25 + V\right)/5.2\right)} \\ \alpha_n\left(V\right) &= \frac{\left(V - 95\right)}{1 - \exp\left(-\left(V - 95\right)/11.8\right)} \qquad \beta_n\left(V\right) = 0.025\exp\left(-\frac{V}{22.2}\right) \quad . \end{aligned} \tag{S.6}$$

Membrane specific parameters are $c_\mathrm{m} = 1\,\frac{\mu\mathrm{F}}{\mathrm{cm}^2}$, $g_\mathrm{Na} = 112.5\,\frac{\mathrm{mS}}{\mathrm{cm}^2}$, $g_\mathrm{K} = 225\,\frac{\mathrm{mS}}{\mathrm{cm}^2}$, $g_\mathrm{L} = 0.25\,\frac{\mathrm{mS}}{\mathrm{cm}^2}$, $V_\mathrm{Na} = 74\,\mathrm{mV}$, $V_\mathrm{K} = -90\,\mathrm{mV}$ and $V_\mathrm{L} = -70\,\mathrm{mV}$.

The Reduced Traub-Miles Pyramidal Neuron Model The reduced Traub-Miles model [5, 6] is defined by

$$\begin{aligned} \frac{d}{dt}V &= I_\mathrm{e} + I_\mathrm{syn} + g_\mathrm{L}\left(V_\mathrm{L} - V\right) + g_\mathrm{Na} m_\infty\left(V\right) h\left(n\right)\left(V_\mathrm{Na} - V\right) + g_\mathrm{K} n^4\left(V_\mathrm{K} - V\right) \\ \frac{d}{dt}n &= \left(1 - n\right)\alpha_n\left(V\right) - n\beta_n\left(V\right) \end{aligned}$$

The steady state functions and time constants are inferred form the rates

$$\begin{aligned} \alpha_m\left(V\right) &= \frac{0.32\left(V + 54\right)}{1 - \exp\left(-\left(V + 54\right)/4\right)} \qquad \beta_m\left(V\right) = \frac{0.28\left(V + 27\right)}{\exp\left(\left(V + 27\right)/5\right) - 1} \\ \alpha_n\left(V\right) &= \frac{0.032\left(V + 52\right)}{1 - \exp\left(-\left(V + 52\right)/5\right)} \qquad \beta_n\left(V\right) = 0.5\exp\left(-\frac{\left(V + 57\right)}{40}\right) \quad . \end{aligned} \tag{S.7}$$

and $h\left(n\right) = \max\left\{1 - 0.25n, 0\right\}$. Membrane specific parameters are $c_\mathrm{m} = 1\,\frac{\mu\mathrm{F}}{\mathrm{cm}^2}$, $g_\mathrm{Na} = 100\,\frac{\mathrm{mS}}{\mathrm{cm}^2}$, $g_\mathrm{K} = 80\,\frac{\mathrm{mS}}{\mathrm{cm}^2}$, $g_\mathrm{L} = 0.1\,\frac{\mathrm{mS}}{\mathrm{cm}^2}$, $V_\mathrm{Na} = 50\,\mathrm{mV}$, $V_\mathrm{K} = -100\,\mathrm{mV}$ and $V_\mathrm{L} = -67\,\mathrm{mV}$.

The Morris-Lecar Neuron Model with Adaptation The model is defined by the Morris-Lecar equations (S.3) [3] with an additional adaptation current

$$I_{\text{adapt}} = g_z z\left(V_z - V\right)$$

and adaptation variable z that evolves as in (S.3) with

$$z_\infty\left(V\right) = \frac{1}{1+\exp\left(\frac{V_\text{a}-V}{V_\text{b}}\right)} \qquad \tau_\text{z}\left(V\right) = 200$$

and parameters as in [7] given by $c_\text{m} = 2\,\frac{\mu\text{F}}{\text{cm}^2}$, $g_\text{Na} = 20.0\,\frac{\text{mS}}{\text{cm}^2}$, $g_\text{K} = 208.0\,\frac{\text{mS}}{\text{cm}^2}$, $g_\text{L} = 2.0\,\frac{\text{mS}}{\text{cm}^2}$, $V_\text{Na} = 50\,\text{mV}$, $V_\text{K} = -100\,\text{mV}$,$V_\text{L} = -60\,\text{mV}$, $V_1 = -1.2\,\text{mV}$, $V_2 = 18\,\text{mV}$, $V_3 = -9\,\text{mV}$ and $V_4 = 10\,\text{mV}$, $\Phi = 4$ and adaptation parameters $V_\text{z} = -100\,\text{mV}$, $V_\text{a} = -30\,\text{mV}$, $V_\text{b} = 5\,\text{mV}$.

Linear Response Theory

We determine the resonance frequency of a general conductance based neuron model from the impedance (or transfer) curve obtained from the linear response to sinusoidal input stimuli. We therefore consider a conductance based neuron model of the form (S.1). We denote a steady state of the dynamics for a constant external current $I_{\text{e},0}$ by $x_0 = \left(V_0, a_{2,0}, \ldots, a_{N,0}\right)^T$, set $I_\text{e} = I_{\text{e},0} + \delta I$ and define

$$\tau_{j,0} = \tau_j\left(V_0\right), \quad g_{k,0} = g_k a_{i_{k,1},\infty}^{l_{k,1}}\left(V_0\right)\ldots a_{i_{k,p_k},\infty}^{l_{k,p_k}}\left(V_0\right) a_{\infty,j_{k,1}}^{m_{k,1}}\left(V_0\right)\ldots a_{\infty,j_{k,q_k}}^{m_{k,q_k}}\left(V_0\right).$$

Linearization around the fixed point in the variables $\delta x = x - x_0$ yields

$$\frac{d}{dt}\delta x = Df\left(x_0\right)\delta x \tag{S.8}$$

or explicitly

$$\begin{aligned} c_m\frac{d}{dt}\delta V &= -g_\text{L}\delta V + \frac{\partial}{\partial V}I_\text{ion}\left(V_0, a_0\right)\delta V + \sum_j \frac{\partial}{\partial a_j}I_\text{ion}\left(V_0, a_0\right)\delta a_j + \delta I\left(t\right) \\ \frac{d}{dt}\delta a_j &= \frac{1}{\tau_{j,0}}\left(a'_{j,\infty}\left(v_0\right)\delta V - \delta a_j\right) \end{aligned}$$

For periodic inputs of the form $\delta I\left(t\right) = I_\delta e^{\iota\omega t}$ with $\iota = \sqrt{-1}$ and $\omega = 2\pi\nu$, we take the following ansatz, $\delta x\left(t\right) = \delta y e^{\iota\omega t}$, where $y = \left(Z, Z_2, \ldots, Z_N\right)^T$. Inserting this into the linearized system (S.8) yields

$$Z_j\left(\omega\right) = \frac{a'_{j,\infty}\left(V_0\right)Z}{\iota\omega\tau_{j,0}+1}$$

and thus for the impedance Z we get

$$Z\left(\omega\right) = \frac{I_\delta}{\iota\omega c_\text{m} + g_\text{L} - \frac{\partial}{\partial v}I_\text{ion}\left(V_0, a_0\right) - \sum_j \frac{\partial}{\partial a_j}I_\text{ion}\left(V_0, a_0\right)\frac{a'_{j,\infty}(V_0)}{\iota\omega\tau_{j,0}+1}} \tag{S.9}$$

For $I_\delta = 1$, this is nothing else than the well know expression for a parallel RCL circuit

$$\frac{1}{Z} = \frac{1}{Z_R} + \frac{1}{Z_C} + \sum_j \frac{1}{Z_j}$$

Close inspection of (S.9) shows that the impedance may be expressed as

$$Z\left(\omega\right) = \frac{\prod_{j=2}^N\left(-\iota\omega - \frac{1}{\tau_{j,0}}\right)}{\det\left(Df\left(x_0\right) - \iota\omega\right)} = \frac{\prod_{j=2}^N\left(-\iota\omega - \frac{1}{\tau_{j,0}}\right)}{\prod_{i=1}^N\left(-\iota\omega + \lambda_i\right)}$$

where λ_i are the eigenvalues of the Jacobian $Df\left(x_0\right)$. From this we have

$$\left|Z\left(\omega\right)\right|^2 = Z\left(\omega\right)\bar{Z}\left(\omega\right) = \frac{\prod_{j=2}^N\left(\tau_{j,0}^{-2} + \omega^2\right)}{\prod_{i=1}^N\left(\lambda_i^2 + \omega^2\right)}$$

The resonance frequency ν_R was determined by the values that maximized $|Z|$, i.e. by $\nu_\text{R} = \arg\max_\nu\left|Z\left(2\pi\nu\right)\right|$. The transition to resonance was detected by numerical continuation of the condition $\frac{d}{d(\omega^2)}\left|Z\left(\omega\right)^2\right|_{\omega^2=0} = 0$, indicating a change from a monotonically decaying to a peaked $|Z|$ at zero frequency. The transitions from real to imaginary eigenvalues (i.e. saddle to focus transitions) were detected by continuation of the zeros of the discriminant for the characteristic polynomial $\det\left(Df\left(x_0\right) - \lambda\right)$.

Supplementary References

[1] Dumortier, F., Roussarie, R., Sotomayor, J., and Zoladek, H. *Bifurcations of Planar Vector Fields: Nilpotent Singularities and Abelian Integrals*, volume 1480 of *Lecture Notes in Mathematics*, (Springer, New York1991).

[2] Wang, X.J. and Buzsáki, G. Gamma oscillation by synaptic inhibition in a hippocampal interneuronal network model. *J. Neurosci.* **16**, 6402–13 (1996).

[3] Morris, C. and Lecar, H. Voltage oscillations in the barnacle giant muscle fiber. *Biophys. J.* **35**, 193–213 (1981).

[4] Erisir, A., Lau, D., Rudy, B., and Leonard, C.S. Function of specific K(+) channels in sustained high-frequency firing of fast-spiking neocortical interneurons. *J. Neurophysiol.* **82**, 2476–89 (1999).

[5] Traub, R.D. and Miles, R. *Neuronal Networks of the Hippocampus* (1991).

[6] Ermentrout, G. and Kopell, N. Fine structure of neural spiking and synchronization in the presence of conduction delays. *Proc. Natl. Acad. Sci.* **95**, 1259–1264 (1998).

[7] Prescott, S.A., Ratté, S., De Koninck, Y., and Sejnowski, T.J. Pyramidal neurons switch from integrators in vitro to resonators under in vivo-like conditions. *J. Neurophysiol.* **100**, 3030–42 (2008).

[8] Rinzel, J. and Ermentrout, G. Analysis of neural excitability and oscillations. In C. Koch and I. Segev, editors, *Methods in neuronal modeling*, 251–291, (MIT Press, Cambridge, MA1989).

[9] Izhikevich, E.M. *Dynamical Systems in Neuroscience*, (MIT Press, Cambridge, MA2010).

[10] Wang, H., Chen, Y., and Chen, Y. First-spike latency in Hodgkin's three classes of neurons. *J. Theor. Biol.* **328**, 19–25 (2013).

[11] Ermentrout, B. Type I membranes, phase resetting curves, and synchrony. *Neural Comput.* **8**, 979–1001 (1996).

[12] Hodgkin, A. The local electric changes associated with repetitive action in a non-medullated axon. *J. Physiol.* **107**, 165–181 (1948).

[13] Murdock, J. *Normal forms and unfoldings for local dynamical systems*, (Springer, New York2002).

[14] Kuznetsov, Y.A. Practical Computation of Normal Forms on Center Manifolds At Degenerate Bogdanov-Takens Bifurcations. *Int. J. Bif. Chaos* **15**, 3535–3546 (2005).

[15] Guckenheimer, J. Multiple bifurcation problems for chemical reactors. *Physica D* **20**, 1–20 (1986).

[16] Guckenheimer, J. and Holmes, P. *Nonlinear Oscillations, Dynamical Systems, and Bifurcations of Vector Fields*, (Springer, New York1983).

[17] Takens, F. Singularities of vector fields. *Publ. Mathématiques l'IHÉS* **43**, 47–100 (1974).

[18] Bogdanov, R. Versal deformations of a singular point of a vector field on the plane in the case of zero eigenvalues. *Funct. Anal. Appl.* **9**, 144–145 (1975).

[19] Dumortier, F., Roussarie, R., and Sotomayor, J. Generic 3-parameter families of vector fields on the plane, unfolding a singularity with nilpotent linear part. The cusp case of codimension 3. *Ergod. Theory Dyn. Syst.* **7**, 375–413 (1987).

[20] Dumortier, F., Roussarie, R., and Sotomayor, J. Bifurcations of cuspidal loops. *Nonlinearity* **10**, 1369–1408 (1997).

[21] Rose, R. and Hindmarsh, J. The assembly of ionic currents in a thalamic neuron I. The three-dimensional model. *Proc. R. Soc. London Ser. B* **237**, 267–288 (1989).

[22] Destexhe, A. and Paré, D. Impact of network activity on the integrative properties of neocortical pyramidal neurons in vivo. *J. Neurophysiol.* **81**, 1531–47 (1999).

[23] Prescott, S.A., De Koninck, Y., and Sejnowski, T.J. Biophysical basis for three distinct dynamical mechanisms of action potential initiation. *PLoS Comput. Biol.* **4**, e1000198 (2008).

[24] Golomb, D., Donner, K., Shacham, L., Shlosberg, D., Amitai, Y., and Hansel, D. Mechanisms of firing patterns in fast-spiking cortical interneurons. *PLoS Comput. Biol.* **3**, e156 (2007).

[25] Acker, C.D., Kopell, N., and White, J.A. Synchronization of strongly coupled excitatory neurons: relating network behavior to biophysics. *J. Comput. Neurosci.* **15**, 71–90 (2003).

[26] Hodgkin, A. and Huxley, A. A quantitative description of membrane current and its application to conduction and excitation in nerve. *J. Physiol.* **117**, 500–544 (1952).

[27] Brown, E., Moehlis, J., and Holmes, P. On the phase reduction and response dynamics of neural oscillator populations. *Neural Comput.* **16**, 673–715 (2004).

[28] Doedel, E.J., Champneys, A.R., Fairgrieve, T., Kuznetsov, Y., Oldeman, B., Paffenroth, R., Sandstede, B., Wang, X., and Zhang, C. Auto-07p: Continuation and bifurcation software for ordinary differential equations, http://indy.cs.concordia.ca/auto (2007).

[29] Champneys, A., Kuznetsov, Y.A., and Sandstede, B. A numerical toolbox for homoclinic bifurcation analysis. *Int. J. Bif. Chaos* **6**, 867–887 (1996).